# Hybrid 3D microfluidic bioprinting for the engineering of cancer models and tissue substitutes

Salvatore D'Alessandro, Sajad Mohammadi, Lucia Iafrate, Marco Bastioli, Martina Marcotulli, Silvia Franco, Biagio Palmisano, Michele D'Orazio, Arianna Mencattini, Roberta Angelini, Mara Riminucci, Franco Marinozzi, Eugenio Martinelli, Giancarlo Ruocco, Fabiano Bini & Gianluca Cidonio

View supplementary material

Published online: 04 Nov 2024.

Submit your article to this journal

Article views: 981

View related articles

View Crossmark data

Taylor & Francis
Taylor & Francis Group

# Hybrid 3D microfluidic bioprinting for the engineering of cancer models and tissue substitutes

Salvatore D'Alessandro [a,b]*, Sajad Mohammadi[b]*, Lucia Iafrate[b], Marco Bastioli[b], Martina Marcotulli[b], Silvia Franco[c], Biagio Palmisano [d], Michele D'Orazio[e], Arianna Mencattini[e], Roberta Angelini[c], Mara Riminucci [d], Franco Marinozzi[a], Eugenio Martinelli[e], Giancarlo Ruocco[b], Fabiano Bini[a]†* and Gianluca Cidonio [a,b]†

aDepartment of Mechanical and Aerospace Engineering, University of Rome "La Sapienza", Rome, Italy; bCenter for Life Nano – & Neuro – Science – CLN2S, Italian Institute of Technology (IIT), Rome, Italy; cInstitute for Complex Systems (ISC-CNR) and Department of Physics, University of Rome La Sapienza, Rome, Italy; dDepartment of Molecular Medicine, University of Rome La Sapienza, Rome, Italy; eDepartment of Information Engineering, Tor Vergata University of Rome, Rome, Italy

**ABSTRACT**
3D bioprinting is at the forefront of tissue engineering to fabricate complex constructs resembling functional tissues. However, the inability to produce heterogeneous tissues and the lack of spatio-temporal control over the release of bioactive factors are greatly limiting clinical translation. Herein, the combination of 3D bioprinting with high-throughput dispensing using a custom microfluidic system and nanoclay-based inks is presented. This approach was found to enhance printability, retention, and controlled release of bioactive factors. Advanced tissue models were developed to resemble cancer and skeletal tissue, while studying the effect of anti-cancer (Doxorubicin) and pro-osteogenic growth factors (bone morphogenetic protein-2, BMP-2), respectively. The engineering of a new nanoclay ink allowed the sustained release, making it suitable for long-term applications. These findings suggest that by combining 3D bioprinting and high-throughput delivery of nanoclay-based inks a new platform for the engineering of functional tissue constructs can be assembled, offering significant advancements in regenerative medicine.
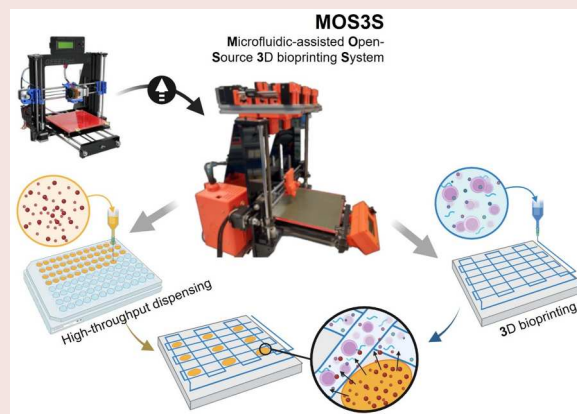
## Introduction

The functional principles of 3D bioprinting are highly intertwined with tissue engineering and regenerative medicine (TERM). Indeed, TERM approaches for tissue repair and modelling have largely relied on the use of 3D bioprinting approaches to assemble biomimetic functional tissues [1,2]. Thus, the ability to create complex, three-dimensional tissue constructs via layer-by-layer deposition of bioinks, which are composite materials containing living cells, biomolecules, and bio-compatible materials, holds great promises for regenerative medicine, drug testing and the development of patient-specific implants [3–6]. However, 3D bioprinting

has not technologically advanced in decades due to the associated number of challenges limiting ultimate application. While current 3D bioprinting techniques can indeed produce heterogeneous and microscale multicellular constructs [7–10], and several commercial bioprinters support multi-ink printing [11–14], a significant limitation remains in terms of cost, customisability, and accessibility. Most advanced bioprinters are expensive and not readily available to a broader range of researchers, particularly in educational settings or smaller laboratories. This financial barrier limits the widespread application of 3D bioprinting in research and development. Therefore, there is a growing need for more affordable bioprinting solutions that maintain advanced functionality while being accessible to a broader range of researchers. To date, the inclusion of compounds of interest is typically carried out by simple dispensing or adsorption of the 3D bioprinted scaffold, or by direct inclusion within the material. The adsorption of compounds of interest onto the implant typically results in poor loading efficiency because of the limited control over grafting to the printed material, leading to uneven distribution, limited interaction with cells with associated poor sustain release [15]. Alternatively, compounds can be incorporated directly within the material ink prior to the bioprinting process. This method ensures that the bioactive compounds are localised within deposited biomatrices, promoting better interaction with the cells and enhancing their effect [7,8]. Additionally, the tuning of the cargo release is influenced by the encapsulation into a single material ink that holds physic-chemical properties ideal for 3D deposition [16]. Studies have shown that the spatial distribution of bioactive compounds is critical for replicating the natural microenvironments of tissues, such as those found in cancer [10–12] and skeletal tissue [17]. Selective spatial patterning can influence cell behaviours, improve tissue functionality, and enhance the relevance of tissue models for research and therapeutic applications. In addition to the composition and spatial distribution of bioactive compounds, the geometry of the scaffold, specifically the precision and accuracy with which the fibres are deposited, plays a crucial role in influencing cellular behaviour as previous studies have shown [18–21]. The engineering of a 3D bioprinting platform for the precise distribution of cells, bioactive factors, and for customised geometries of the scaffolds opens new avenues for the fabrication and the rapid prototyping of readily functional tissue constructs.

The newly developed Microfluidic-Assisted Open-Source 3D Bioprinting System (MOS3S) offers a solution to the limitations offering a precise dispensing, refers to the high-throughput technique used to deposit droplets of biomaterials within the scaffold's porosities, and printing capabilities at the same time, refers to the deposition of material to construct the scaffold [22]. The MOS3S system has been adapted to alternately dispense bioactive compounds and deposit biomaterial inks, allowing for the creation of complex and functional tissue constructs. While MOS3S system retains the advanced features of high-end 3D bioprinters, the material inks traditionally used in 3D bioprinting remain not suitable for long-term compartmentalisation of bioactive factors. Nanoclay dispersions present a promising solution to these limitations when blended with other polymer components, as previously reported [15,16,23,24]. Indeed, even at low weight-volume concentrations, clay nanoparticles are effective for drug localisation with functional biocompatible properties [25]. The use of nanoclay allows for dose-dependent control over the retention of bioactive factors, without drastically altering the biocompatible properties. Studies have shown that by increasing the amount of nanoclay in the material, the direct retention and sustained localisation can be preserved over a prolonged period of time [23,24]. Furthermore, the inclusion of nanoclay has been found beneficial for the enhancement of the printability of a number of polymers used for skeletal regeneration [26,27]. However, the possibility to independently control drug release and tissue formation following nanoclay-based bioinks deposition is still missing and potentially beneficial to enhance tissue fabrication and TERM approaches.

In this study, a library of nanoclay-based and nanoclay-free materials has been printed with MOS3S to produce advanced tissue models. A novel approach based on coaxial microfluidic-based extrusion and 3D bioprinting, jointly with high-throughput dispensing is here reported for the first time in combination with nanoclay-based bioinks. Harnessing the intrinsic macro-porosity of 3D bioprinted cell-laden constructs, we have demonstrated the possibility to pattern compartmentalised nanocomposite microdroplets including various biologics for sustained release purposes. Thus, functional tissue constructs have been fabricated inspired by the modelling of cancer or skeletal tissues. Particularly, cancer models have been engineered by 3D bioprinting with the precise compartmentalisation of anti-cancer drugs for safety and efficacy studies, towards drug testing and development. Similarly, skeletal substitutes have been bioprinted by delivering skeletal stem cells in 3D, while concomitantly dispensing growth factor of interest alongside the macropores. This targeted approach holds the potential to drive further bone tissue formation, offering potential applications in regenerative medicine and orthopaedics.

## Material and methods

### Materials

Ru-Tris(2,2'-bipyridyl) dichloro-ruthenium(II)hexahydrate (cat no. 224758), Sodium persulfate (SPS) (cat no. 216232), Gelatin – type A porcine skin (~300 g bloom) (cat no. G1890), Methacrylic anhydride (cat no. 276685), phosphate buffered saline (PBS), Hanks' balanced salt solution (HBSS) and Dulbecco's Modified Eagle's Medium (DMEM) high glucose were purchased from Sigma-Aldrich. LAPONITE®-XLG provided by BYK, UK. Naphthol AS-MX Phosphate Alkaline Solution by Simga 85-5. Fast Violet Salt by Sigma F1631. Alginate Lyase enzyme by Merck-Sigma. Dextran FITC (from Leuconostoc spp., Mr ≈ 70 000). Recombinant Human Vascular Endothelial Growth Factor-A (rh VEGF-A) provided by ImmunoTools. Vybrant™ DiD Cell-Labeling Solution provided by Thermo Fisher Scientific. Calcein AM (ThermoFischer, C3099).

### Synthesis of Gelatin Methacryloyl (GelMA)

Gelatin methacryloyl (GelMA) was synthesised following a previously reported process [28,29]. Briefly, gelatin (type A3, ~300 Bloom from porcine skin) was dissolved at a 10% (w/v) concentration in PBS (pH 7.5/8) at 50℃. Methacrylic anhydride (MA, 0.8 ml per gram of gelatin) was added to the gelatin solution dropwise under vigorous stirring for 3 h. Following this step, the solution was dialyzed against deionised water (DW) using 1–2 kDa cut-off dialysis tubes for ~5 days at 50℃ [30–32]. Finally, GelMA was lyophilised and kept at 4 ℃ for further use.

### Preparation Alginate-GelMA and nanocomposite inks

Alginate (A) and GelMA (G) were sterilised under UV light for 30 min and subsequently dissolved in DW under constant stirring at 40℃ for 3 h. Two distinct AG ink blends were prepared, maintaining a fixed GelMA concentration while varying the alginate concentration. These blends were designated varying the concentration of alginate as low concentration alginate (l-AG) with a composition of 2% A and 1.5% G (w/v), and high concentration alginate (h-AG) with a composition of 4% alginate and 1.5% GelMA (w/v). Nanocomposite inks were prepared by sterilising for 30 min under UV light the powder content of nanoclay (n, Laponite®), alginate, and GelMA. Laponite® was slowly added to DW under stirring. After 2 hours, A and G were added following the same procedure used for the preparation of the AG inks. The resulting blend, designated as nanoclay low concentration alginate (n-l-LAG), consisted of 0.5% nanoclay, 2% A, and 1.5% G (w/v).

### Rheological investigation of printable inks

Rheological properties of the alginate-GelMA and nanocomposite inks were analysed using a rotational rheometer (Anton Paar MCR 302) at 25℃ equipped with a cone-plate geometry (25 mm diameter, 1° cone angle). Temperature control was maintained by a Peltier system, and solvent evaporation was prevented by saturating the atmosphere surrounding the sample with water and by using an evaporation blocker around the plate and an isolation hood. The shear viscosity behaviour of the samples was assessed by applying a shear rate from 1 to 100 $s^{-1}$ during measurements.

### Investigation of inks printability and 3D scaffold geometric properties

To evaluate the structural stability of the printing material and ensure fidelity between the printed constructs and the desired designs, a bridge test was conducted. This test aimed to observe whether the weight of the material causes deformation of the filament, as proposed by Ribeiro et al. [33]. The procedure involved printing filaments over supports with increasing gaps, starting from 1 mm and extending to 5 mm in 1 mm increments. The GANYMEDE-II-HR – High-Resolution, Video-Rate Spectral Domain Optical Coherence Tomography (OCT) Imaging System, 900 nm (Thorlabs Inc., Dachau, Germany) was used to collect images of the printed scaffold and verify stability. Using the Thorlabs system, an axial resolution of approximately 6 μm and a lateral resolution of 8–15 μm were achieved. Images of the lattice scaffolds, with the initial 4 layers were printed with a pore size of 0.5 mm and a scaffold size of 9×9 mm to establish a foundational support structure, then 8 additional layers were printed with a pore size of 3 mm each. Post-printing was acquired using a ZEISS Stemi 305 Compact Stereo Microscope with 5:1 Zoom, and the photos were subsequently analysed with Image J software to measure their geometric characteristics such as overall dimension, strand width, spread ratio and pore size, identifying ideal results with dotted lines.

### Scanning electron microscopy (SEM)

SEM micrographs were acquired from acellular printed scaffolds to study the microstructure of the different blends of materials. Prior to SEM imaging, samples

were lyophilised and visualised using SEM. The micrographs of cross-sectioned lyophilised samples were taken at 10 kV voltage at varying magnification (100x, 200x).

### Controlled 3D deposition of material inks

The printing process was carried out using an custom microfluidic-assisted open-source 3D bioprinting system (MOS3S) [22] previously developed, using a coaxial nozzle, with inner and outer diameters of 25G and 18G, respectively. A custom-made G-code was employed to create porous and lattice scaffolds. The integration of 3D-printed syringe pumps with the motion control system allowed the implementation of high-throughput technology, which was used in two different experiments: one to release ink droplets into scaffold pores and another to extrude specific volumes into well plates, enabling efficient high-throughput experimentation. Specifically, 3D-printed scaffolds, as shown in **Video 1**, depositing 4 layers at a layer height of 240 μm with a fibre spacing of 0.5 mm, followed by an additional 16 layers at a layer height of 120 μm and a fibre spacing of 3 mm to create large pores, and 2 μL droplet of filler was deposited inside the large pores using the high-throughput process. A 0.33 M $CaCl_2$ solution along with ruthenium (Ru) at a concentration of 0.3 mM/ml and sodium persulfate (SPS) at 3 mM/ml were employed for crosslinking during the printing process.

### High-throughput patterning and drug release study

The high-throughput process was performed using the MOS3S 3D bioprinter with high-throughput patterning capabilities, controlled by ad-hoc G-Code to coordinate nozzle movement and syringe pump extrusion, allowing for the deposition of nanocomposite inks from 10 to 300 μl per well into a 96-well plate. The resolution of the syringe pumps was investigated by validating the volume deposited within each well. Nanocomposite inks coloured differently were used to validate the gradient control over high-throughput deposition with a custom G-code. Release from nanoclay-based (n-l-AG) and nanoclay-free (h-AG) deposited inks was evaluated using FITC-Dextran. Specifically, FITC-Dextran was solubilised in n-l-AG and h-AG at a concentration of 10 μg/mL, and 100 μL of the material was used as samples, which were crosslinked with Ru/SPS. Specifically, the small cylinders (n=3) were soaked in 100 μL of HBSS for 1, 2, 3, 6, 24, 48, 96, 120 and 144 hours, and the fluorescence emissions were measured to quantify the drug release. To estimate the drug concentration, a calibration curve was established using FITC-Dextran concentrations ranging from 0 to 10 μg/mL, in increments of 1 μg/mL, dissolved in HBSS. Fluorescence emission of these calibration samples of 100 μL was measured to generate a regression line. The measurements of fluorescence emission of FITC-Dextran samples were performed using a Tecan i-control infinite 200Pro, employing a Thermo Fisher Scientific-Nunclon 96 Flat Bottom Black well plate. Each well was read four times (Multiple Reads per Well) with an excitation wavelength of 485 nm and an emission wavelength of 535 nm. The device was set to perform 25 flashes per reading at a controlled temperature of 25℃. The picture acquisition of samples was taken with Carl Zeiss™ Axio Vert.A1 FL-LED Inverted Microscope exciting the FITC-Dextran in green fluorescent protein led.

### Cell isolation, encapsulation, and printing

#### Cancer cells deposition with Doxorubicin patterning

MDAMB-231 (ATCC, USA) P6 were plated in cell culture flasks with DMEM supplemented with 10% (volume fraction) fetal bovine serum (FBS), 1% (volume fraction penicillin and 1% (volume fraction) streptomycin (Pen/Strep) and maintained at 37℃ and 5% $CO_2$ balanced air. Cells were passaged at approximately completed confluency and treated with trypsin. The MDAMB-231 were used for experimental use at passage seven. The cells were suspended at a density of $1\times10^6$/ml in serum-free culture medium and labelled with Vybrant DiD following manufacturer protocol and as previously reported [16]. Briefly, the cell suspensions supplemented with DiD at 5 μL/ml were incubated for 20 min at 37℃ and then centrifugated to remove the supernatant. Then, the cells were suspended in 50 μL of serum-free culture media and added to the material ink which was mixed by pipetting. The bioink was extruded through a 25G nozzle and after printing the scaffold was incubated at 37℃ and 5% $CO_2$ balanced air. Then, two methods were used to administer the doxorubicin: (i) one-time dosage delivery with the dispersion of 2 μM Doxorubicin within the culture media for 24 hours, and (ii) sustained exposure method, encapsulating 2 μM of anti-tumour drug in printed n-l-AG droplets on the scaffold.

#### Skeletal stem cells deposition with bone morphogenetic protein-2 patterning

Human bone marrow stromal cells (HBMSCs) were isolated as previously described [34]. Briefly, bone specimens were collected as surgical waste from healthy subjects undergoing orthopedic surgery. Bone

fragments were minced and rinsed with culture medium in order to release bone marrow cells. After vigorous pipetting, cell suspensions were filtered through a 70 µm nylon mesh cell strainer and cultured in Minimum Essential Medium with alpha modification (Merck Life Sciences, Saint Louis, USA) supplemented with 20% FBS (Thermo Fisher Scientific, Waltham, USA), 1% Penicillin/Streptomycin (Merck Life Sciences) and 1% L-glutamine (Merck Life Sciences). Cells P2 were seeded at the density of $2 \cdot 10^5$ cells/cm$^2$ and grown at 37°C in a 5% $CO_2$ controlled atmosphere. Cells were passaged at approximately completed confluency and treated with trypsin-EDTA 1X. HBMSCs were used for experimental use in passage two. The cells were suspended in 50 µL of serum-free culture media and added to the material ink which was mixed by pipetting gently. The bioink was extruded through a 25G nozzle and after printing the scaffold was incubated at 37°C and 5% $CO_2$ balanced air. The BMP-2 was administered with a sustained exposure method encapsulating the growth factor, with a concentration of 5 µl/ml, in printed n-l-AG droplets on the scaffold.

### Viability and proliferation of cell-laden printed scaffolds

Viability at day 1 and 7 was investigated using Calcein AM staining and confocal imaging following a previously reported method [35]. Briefly, samples were washed twice with HBSS. Calcein AM was diluted in serum-free culture media and added to cell-laden scaffolds. Constructs were incubated at 37°C and 5% $CO_2$ balanced air for 1 h. Then, samples were washed three times with HBSS. Samples were imaged using a confocal scanning microscope (Olympus IX83) with a 10x magnification objective. Living cells were identified when stained with Calcein AM and DiD. Metabolically inactive (dead) cells were identified by DiD staining. Analysis was carried out using ImageJ. Cell density was calculated by normalisation of viable cells and the volume of interests. Proliferation was subsequently quantified as the percentage change in cell viability from day 1 (set at 100%) to day 7 providing a direct measure of cellular proliferation within the scaffolds over the study period.

### Alkaline phosphatase staining and imaging on culture plate

Scaffolds were first removed from the culture medium and washed twice with HBSS. A 95% ethanol aqueous solution was then applied to the scaffolds for 10 minutes, followed by two additional washes with HBSS. The scaffolds were allowed to dry overnight in a refrigerator for drying. After, a staining solution was prepared with 0.04% Naphtol AS-MX Phosphate Alkaline Solution and 24 mg/mL Fast Violet Salt in water. This solution was applied to the scaffolds, which were then incubated at 37°C for 60 minutes. Following incubation, the scaffolds were rinsed with water, and images were captured using a Carl Zeiss™ Axio Vert.A1 FL-LED Inverted Microscope in transmission mode.

### Polymerase chain reaction (PCR)

HBMSCs P2 were seeded in two Falcon® 175cm$^2$ flask with an initial seeding concentration of $2.8 \cdot 10^3$ cells/cm$^2$, medium change was performed twice a week with MinimumEssential Medium with alpha modification (Merck Life Sciences, Saint Louis, USA) supplemented with 20% Fetal Bovin Serum (Thermo Fisher Scientific, Waltham, USA), 1% Penicillin/Streptomycin (Merck Life Sciences) and 1% L-glutamine (Merck Life Sciences). After 10 days of culture cells were harvested by using trypsin-EDTA 1X for 5 min at 37°C and then, cellular suspension was centrifuged at 1500 rpm for 10 min. Supernatant was discharged and the pallet was resuspended with culture medium with a concentration of $1 \cdot 10^6$ cells/ml. $0.5 \cdot 10^6$ cells were collected in a 1.5 ml LoBind® Eppendorf in the corresponding suspension volume to analyse as D0 control for a gene expression analysis. Cellular suspension was centrifuged again with an ultracentrifuge at 1500 rpm for 10 min to remove culture medium. Finally, cellular pellet was lysed adding 350 µL TRK lysis buffer supplied by E.Z.N.A.® Total RNA Kit (VWR) and then samples were stored and freezed at -80°C for 7 days. The remaining cellular suspension was centrifuged again and encapsulated with a concentration of $3 \cdot 10^6$ cell/ml in n-l-LAG, then a triplet of scaffolds for each condition, both with BMP-2 and without BMP-2, was bioprinted. Samples after 7 days of culture in basal medium were analysed to evaluate gene expression. Firstly, three samples without BMP-2 controls and three samples with BMP-2 were prepared for RNA extraction. An initial material dissolution was performed to obtain a better quality of RNA: samples with BMP-2 and without BMP-2 were added into a 2 ml Eppendorf Low Bind and a solution of Collagenase D at 1 mg/ml and Alginate Lyase at 1:5 dilution in PBS was added for 2 h at 37°C. Samples were then centrifuged at 1500 rpm for 10 min to remove the supernatant. A last incubation with Bovin Serum Albumin (BSA) at 60 mg/ml was carried out at 37°C for 30 min At the end of the incubation samples were centrifuged at 1500 rpm for 10 min to remove the supernatant. RNA extraction was carried out by adding 500ul of TRIzol® reagent (Thermo Fischer

Scientific) following the protocol provided by the supplier: 0.5 ml of TRIzol reagent was added into each sample by pipetting and, after 5 min of incubation, lysate was transferred into a RNAse-free tube. 100 μl of Chloroform were added in each Eppendorf and, after vortexing, samples were incubated for 3 mins at RT. Samples were spinning down at 11000x g for 15 min at 4°C and the final aqueous phase was transferred to a fresh microcentrifuge tube. Finally, a volume of 70% ethanol was added to the lysate by pipetting. After this preliminary step, samples were centrifuged at 10,000 g at 4°C and followed E.Z.N.A.® Total RNA Kit protocol for DNASE, and then they were washed with wash buffer I and wash buffer II. At the end, the spin column was placed in a new 1.5 ml collection tube and to elute RNA 30–50 μl of RNase-free water were added directly and gently to the spin column membrane. Samples were centrifuged for 2 min at full speed and at 4°C, and quantified by using Nanodrop 2000c, Thermo Scientific. After the quantification, RNA sample can be stored at -80°C. For cDNA synthesis, Prime-Script™ RT reagent Kit (Takara) was used. For each RNA sample, 100 ng of RNA were converted into cDNA by following the kit protocol. PCR Eppendorf Tube (Starlab) 0.2 ml were used for the reactions, which was carried out using a thermocycler, Applied Biosystems 2720. Thermal cycle settled on thermocycler: 15 min 37°C, 5s 85°C, hold 4°C. The obtained cDNA was used to detect the main osteogenic genes on day 0, day 7. To perform RT-qPCR, cDNA previously synthesised were diluted in a concentration of 2 ng/ml and then the RT-qPCR reactions were carried out on a 96-well PCR plate (Starlab), by using a solution composed of SYBR iTaq Universal Green Supermix (Bio-rad), cDNA, PCR oligonucleotides (Sigma-Aldrich), and DW. Glyceraldehyde triphosphate dehydrogenase (GAPDH) was analysed as endogenous gene, then the osteogenesis was investigated with the expression of runt-related transcription factor 2 (RUNX2), osterix (OSX), alkaline phosphatase (ALP), type I collagen alpha 1 (COL1A1), osteocalcin (OCNv2), bone morphogenic protein 2 (BMP2). The Primers sequence was reported in Table 1. For each sample of cDNA, a triplicate control was analysed. After the first phase of the reaction preparation,

PCR plate was inserted into the Real-time PCR machine, Applied Biosystems was set the following thermal cycle (x40): Hold 30s at 95°C, 15 min at 95°C, 1 min at 60°C.

## Chick embryo chorioallantois membrane (CAM) procedure

Animal procedures were strictly regulated by European Directive 2010/63/EU and by Italian Legislative Decree No. 26 dated 4th March 2014. The implantation method on the CAM was carried out following a previous reported process [27, 36]. At Day 0 chicken eggs were incubated in a Cimuka CT120SH incubator (Ankara, Turkey) for 14 days at 37.7°C in a 50% humified atmosphere while turning 90 degrees every 2 h. At Day 7 of incubation, a scalpel was used under sterile conditions to create a 1 cm$^2$ window on the eggshell. A total of six eggs per treatment group were used. Scaffolds were printed using sterile n-l-AG ink either comprising HBMSCs (control) or both cells and growth factors. The latter group was fabricated by 3D bioprinting HBMSCs followed by the deposition of filler material within pores with 10 μg/ml VEGF. Every scaffold was driven through the window in a flat position and was accurately placed over the CAM. The eggs were sealed with sterile parafilm, incubated without rotation and daily checked. At Day 14 of incubation, scaffolds were harvested, and CAM integration was inspected with a stereomicroscope with a digital camera, subsequently, the gestational process was terminated under specific guidelines.

## AI analysis

The dataset for CAM assay was composed of images of chick embryo chorioallantoic membrane vessels either with or without 3D bioprinted construct acquired with a Zeiss Stemi 305 stereomicroscope at 1x magnification. A total of three images per experimental condition: Control, i.e., comprising n-l-AG ink with HBMSCs, VEGF, i.e., n-l-AG ink with HBMSCs and a filler material with 10 μg/ml VEGF, and empty, i.e., no bioprinted construct. The performed analysis can be divided into the following parts: vessel segmentation, Area and diameter computing, and Chalkley score (CS) calculus.

### Vessels segmentation

The image analysis was conducted in Matlab 2024a®. Vessels were segmented using Segment Anything Model (SAM) [37] with foreground and background points as prompts. This stage outputs binary images with true (false) values in pixels belonging (not

**Table 1.** Primers sequences.

| Gene | Forward | Reverse |
|------|---------|---------|
| RUNX2 | GTAGATGGACCTCGGGAACC | GAGGCGGTCAGAGAACAAAC |
| OSX | ATGGGCTCCTTTCACCTG | GGGAAAAGGGAGGGTAATC |
| ALP | GGAACTCCTGACCCTTGACC | TCCTGTTCAGCTCGTACTGC |
| COL1a1 | GAGTGCTGTCCCGTCTGC | TTTCTTGGTCGGTGGGTG |
| OCNv2 | AAGAGACCCAGGCGCTACCT | AACTCGTCACAGTCCGGATTG |
| BMP2 | TCAAGCCAAACACAAACAGC | AGCCACAATCCAGTCATTCC |
| GAPDH | GACAGTCAGCCGCATCTTCTT | TCCGTTGACTCCGACCTTCA |

belonging) to vessels. Each separated vessel (in the 8-connection sense) is then identified, with *bwlabel* function, and analysed. In the empty class, a central region corresponding to the average area of a bioprinted construct is removed (set to background) to avoid a bias in the computing of vessel diameter, area, and CS.

### Area and diameter computing

The area is extracted by summing the number of non-zero pixels for each object. The following steps are applied to compute the diameter. The binary image is complemented, and the distance from the first non-zero pixel is computed for each pixel using the *bwdist* function. This ensures that the value at the centre of each vessel represents its radius. The positions of the pixels identifying the centre of the vessels are obtained by skeletonising the original binary image using the basket function. The obtained list of radii is then multiplied by two to get diameters, and the lowest values, below the 5$^{th}$ percentile for each vessel, are removed to account for the ending parts of the vessels.

### Chalkley score computing

The Chalkley score (CS) is calculated automatically in an interactive framework [38]. The user is asked to draw a bounding box containing the bioprinted construct: this information is used to centre and scale the Chalkley grid. CS is then computed by counting the number of circles in the Chalkley grid that intersect at least one vessel in the image. CS is obtained at different rotation angles of the Chalkley grid from 0° to 360° with step 10°. Only the ten highest CS values are considered for each image.

### Statistical analysis

GraphPad Prism 7 (GraphPad Software Inc., La Jolla, CA) was used for statistical analysis. D'Agostino–Pearson normality test was used to assess the differences in the data. Non-significant differences were defined as $p > 0.05$. When multiple comparison tests were performed for the data analysed using one-way and two-way analysis of variance, a correction using Sidak or Tukey testing was carried out.

## Results and discussion

To date, 3D bioprinting has offered a versatile support for the development of tissue-engineered constructs [39]. However, the inability to process multiple tissues in a single print, as well as the lack of current ability to compartmentalise compounds of interest is greatly limiting further development of this technology [20]. Here,

we have investigated the possibility to combine 3D bioprinting and high-throughput dispensing approaches for the fabrication of hierarchical constructs for regenerative medicine and disease modelling purposes. A microfluidic-assisted open-source 3D bioprinting system (MOS3S) previously developed [22] was equipped with a coaxial nozzle for *in-situ* crosslinking strategy (Figure 1(a)), featuring a 25G inner nozzle and an 18G outer nozzle, facilitating the simultaneous extrusion of two solutions, respectively an alginate-GelMA-based ink and the crosslinker solution with $CaCl_2$. The MOS3S custom system is equipped with three syringe pumps, which enable the controlled extrusion of multiple materials simultaneously, offering a broad range of applications, high-throughput capabilities, and versatile 3D bioprinting.

A library of material blends was screened to identify the optimal combination for 3D bioprinting purposes. Specifically, to engineer a three-dimensional platform, we selected alginate, GelMA, and Laponite® for their unique and complementary properties. Alginate was chosen to facilitate the printing process by enabling crosslinking directly at the deposition site [40], thereby providing the necessary structural integrity for the printed constructs [41]. GelMA was integrated to enhance the biomimetic properties of the material, improving cell adhesion, proliferation, and differentiation [42–44]. Lastly, Laponite® was incorporated due to its excellent biocompatible properties and the ability to modify the ink rheology, making it a suitable component for TERM applications as shown in previous studies [26,45–47]. By combining these materials, we aimed to engineer a multifunctional bioink capable of meeting the diverse requirements of both disease modelling and tissue repair. In fact, we aimed to engineer a 3D printed cellular construct to possess excellent printability, ensuring ease of reproducibility, specific degradation properties, controlled substance release, and high biocompatibility.

To identify the best candidate for this, we investigated the printability properties of distinct blends of materials. A low concentration alginate-GelMA (l-AG), consisting of 2% (w/v) alginate and 1.5% (w/v) gelatin methacrylate (GelMA) (Figure 1(b) was prepared and tested for printing fidelity (Figure 1(b), i–v) resulting capable of preserving shape following deposition. By using a greater concentration of alginate (4% w/v) a high-concentration alginate-GelMA (h-AG) was engineered (Figure 1(c)) demonstrating a superior ability to being deposited with a coaxial approach. However, to preserve the low-concentration of polymer content, which has been demonstrated beneficial for cell inclusion and viability [27], nanoclay-enhanced
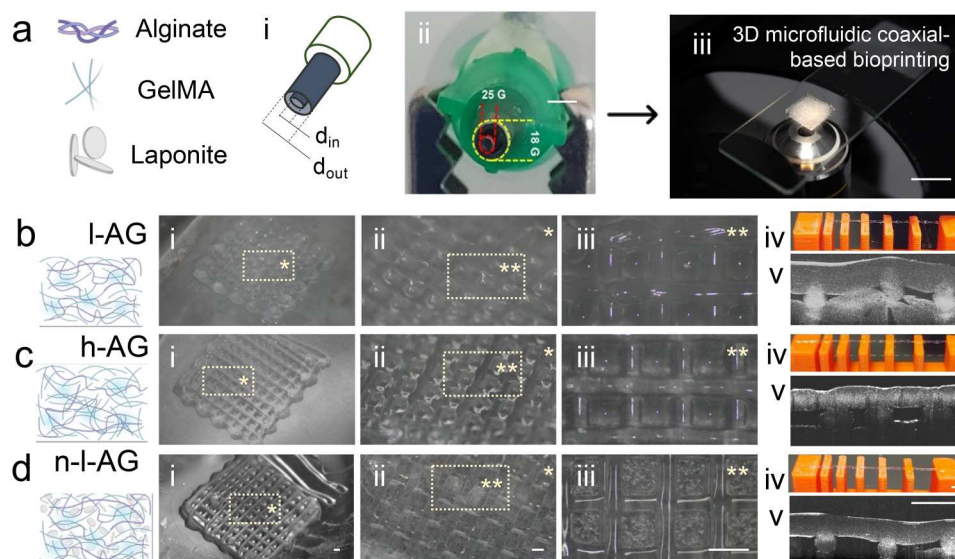
**Figure 1.** (a) Display of the three materials, alginate, gelMA, and laponite used to create the three ink blends for cell culture, a schematic of the coaxial nozzle (i), a photo showing the concentric nozzles were the inner diameter is 25G and the outer is 18G (ii), and a picture of a printed scaffold (iii). b) Scaffold printed with l-AG material showing a lattice structure with 10 mm side and 1 mm fibre spacing (i–iii) and it maintained structural integrity in the bridge test, spanning 5 mm without collapsing (iv–v). c) Scaffold printed with h-AG material demonstrating a similar lattice structure and accurate 10 mm size reproduction (i–iii) and successfully passed the bridge test, demonstrating notable stability over spans of up to 5 mm (iv–v). d) Scaffold printed with n-l-AG material illustrating superior printability (i–iii), fidelity to the lattice design, and accurate 10 mm size reproduction exhibiting an impressive support in the bridge test, sustaining spans of 5 mm effectively (iv–v). Scale bars: (a,iii) 10 mm, (b-d) 1mm.

alginate-GelMA (n-l-AG) was prepared by adding a low percentage of nanoclay to the l-AG ink. This resulted (Figure 1(d)) in an improved printability and stability during the filament hanging test and OCT compared to the l-AG control. These investigations confirmed that the use of nanoclay can readily enhance the printability of extrusion-based approaches [26], including coaxial-assisted deposition. SEM imaging was conducted to investigate the microscopic structure of the different gel compositions reported in the supplementary information (SI) as shown in Figure S1. The images, captured at 100x and 200x magnifications, reveal distinct microstructural differences between the gels. The l-AG material (Figure S1a) exhibits a highly porous structure with large pores and relatively smooth superficial regions. In contrast, the h-AG material (Figure S1b) shows a structure with predominantly small pores and fewer visible smooth areas, possibly due to the higher polymer content. The n-l-AG material presents a hybrid microstructure (Figure S1c), characterised by medium-sized pores along with a crinkled surface and small porosities. The inclusion of nanoclay has possibly remodelled the low polymeric content, providing the opportunity to modulate the internal porosities based on the nanosilicate content. These observations highlight the varied microstructural properties of the materials, which may influence their mechanical

performance and interaction with cells, particularly in terms of porosity and surface morphology.

The 3D scaffolds fabricated with these material inks resembled a lattice structure with a side length of 10 mm and a fibre spacing of 1 mm (Figure 2(a)). The intrinsic stability of the material library was evaluated by studying the mass loss percentage of the printed constructs. Consistently, the ink with the lowest percentage of polymer content (l-AG) was found to lose a larger quantity of mass compared to the material with the highest polymer content (h-AG). Noticeably, the inclusion of nanoclay helped to reduce the degradation rate over 21 days, confirming the hypothesis that Laponite® might aid ink stability following extrusion (Figure 2(b)). These results indicate that n-l-AG possesses the best stability and durability among the three materials and the l-AG is characterised by the highest mass loss during the time. To investigate the ability of the ink to withstand extrusion, rheological properties were investigated. The resulting viscosity-shear rate curves revealed that the inclusion of nanoclay within the l-AG ink was found to positively affect overall viscoelastic properties (Figure 2(c)). At low shear rates, n-l-AG exhibited the highest viscosity, indicating strong structural integrity and resistance to flow. As the shear rate increased, the viscosities of both h-AG and n-l-AG converged to similar values, demonstrating comparable flow
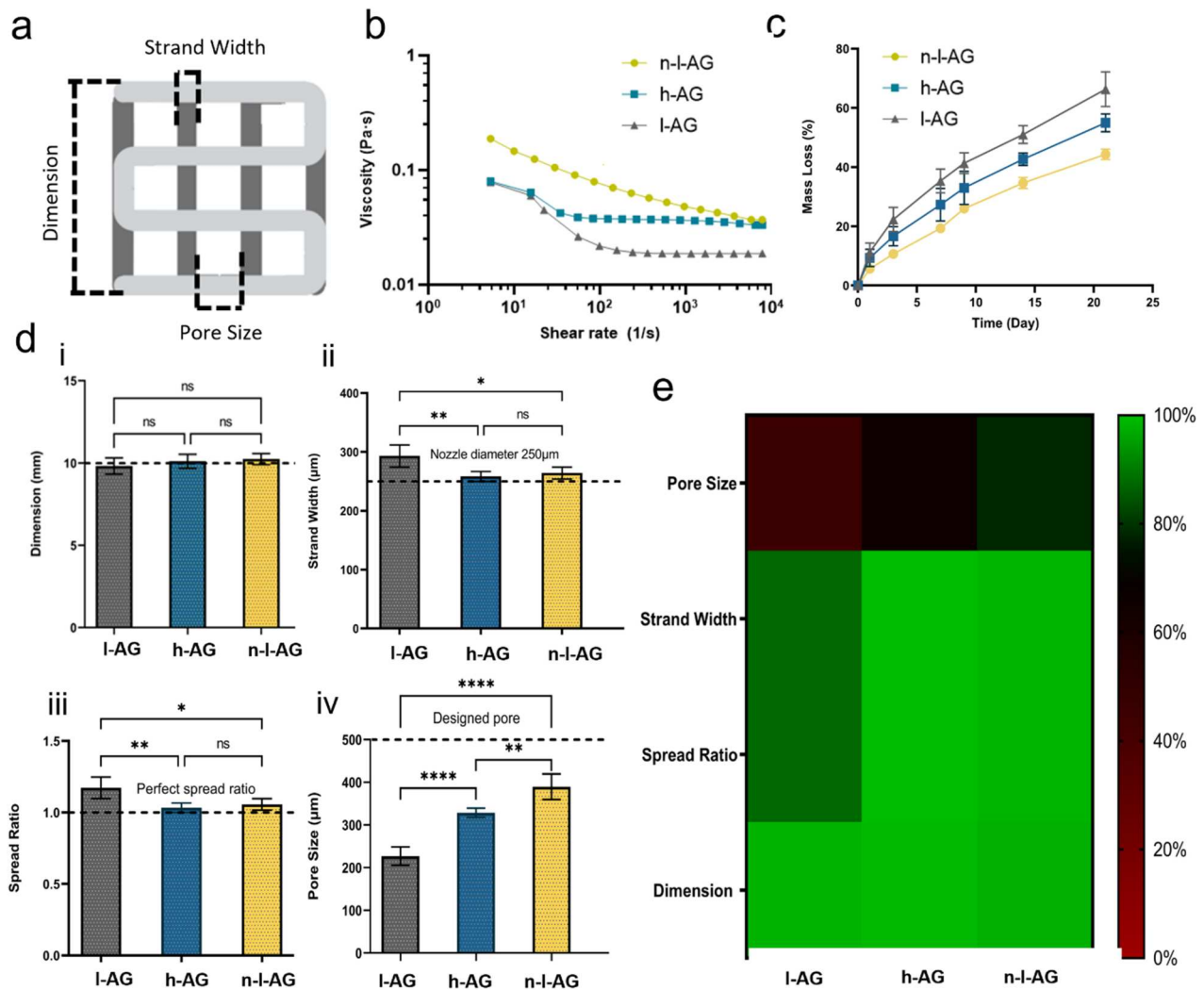
**Figure 2.** (a) Pictures of printed l-AG, h-Ag, and n-l-AG scaffolds. (b) Plot of mass loss from the printed scaffolds over time (days 1, 3, 7, 9, 14, 21), showing n-l-AG with the lowest mass loss (42% at 21 days), followed by h-AG (50%), and l-AG (60%). (c) Viscosity as a function of the shear rates at 25 oC for the three materials, with n-l-AG showing the highest viscosity at low shear rates, and h-AG and n-l-AG converging at higher shear rates; l-AG remains lower across all shear rates. (d) Measurement of strand width compared to the theoretical nozzle diameter (250 μm), showing that all materials produce fibres close to this diameter, with l-AG fibres slightly larger at approximately 300 μm. (e) Measurement of scaffold dimensions demonstrating that l-AG, h-AG, and n-l-AG each successfully achieved the intended 10 mm size, confirming the consistency in size reproduction across all materials. (f) Spread ratio of the printed fibres compared to the nozzle diameter (250 μm), with l-AG showing a ratio greater than 1 due to its softness, while h-AG and n-l-AG maintain a ratio close to 1. (g) (f) Colorimetric summary of the properties of the three materials, with red indicating poor performance and green indicating excellent performance for each characteristic. Mean ± S.D, *n*=5, *$p<0.05$, **$p<0.01$, ****$p<0.0001$.

behaviours under high shear conditions, and indeed showing greater control during the printing phase. In contrast, the viscosity of l-AG remained consistently lower across all shear rates, reflecting its softer nature and worse printability properties. This was clearly visible for the bioprinted constructs. Moreover, this was also confirmed by plot of stress respect of shear rate as shown in Figure S2, only the sample l-n-AG is characterised by a yield stress σy = (0.7 ± 0.1) Pa (Table S1 in SI), sustaining the idea that the material flows with a certain resistance with respect to the others. Following the detailed analysis of viscoelastic properties, it is evident that the superior printability of the n-l-AG ink can be attributed significantly to its yield stress. The n-l-AG ink shows the ability to maintain a specific form under low shear conditions while flowing adequately under higher shear, a critical balance for effective 3D bioprinting [33,48,49]. This yield stress ensures that n-l-AG not only supports its own weight during layering but also minimises spreading after deposition, crucial for achieving high-resolution and structurally intricate bioprinted constructs. Following

deposition, image acquisition and analysis revealed that the three material inks demonstrated the capability to be printed successfully into the desired lattice structures. A number of key parameters were assessed following the extrusion of the material inks in the analysis. All three materials were evaluated for their ability to reproduce the intended scaffold dimensions accurately (Figure 2(d),i). The target size for the scaffold was set to 10 mm. Measurements confirmed that all materials inks successfully achieved this lateral dimension. This consistency in size reproduction indicates that the customised 3D bioprinting platform can reliably produce scaffolds of the desired dimensions, regardless of the material composition. This capability is crucial for ensuring the structural integrity and uniformity of the scaffolds in various biomedical applications. Additionally, the thickness of the printed filaments (Figure 2(d), ii) was compared to the theoretical value corresponding to the diameter of the nozzle used for printing, set at 250 µm. All three materials demonstrated the capability to reproduce fibres with dimensions close to the internal diameter of the nozzle. However, it was observed that the l-AG produced larger fibres of approximately 300 µm in diameter. This discrepancy is attributed to the softness of the material, which causes it to spread and settle on the deposited layer, resulting in fibres that do not maintain a perfect cylindrical shape. The analysis of the spread ratio (Figure 2(d),iii), which is defined as the ratio between the deposited fibre diameter and the nozzle diameter, provides important insights into the printability of the different materials. For l-AG the spread ratio is observed to be greater than the standard value. This is possibly due to the soft nature of the l-AG material which tends to increasingly flatten out upon deposition, resulting in a fibre diameter that exceeds the nozzle diameter. This spreading behaviour can be attributed to the lower viscosity and structural integrity of the l-AG material, which causes it to spread more readily when it contacts the printing surface. In contrast, the spread ratios for h-AG and for n-l-AG are both close to the ideal value. This indicates that these materials maintain their cylindrical shape more effectively upon deposition, closely matching the nozzle diameter. The higher viscosity of h-AG and n-l-AG demonstrated in Figure 2(b) was found to facilitate the prevention of excessive spreading, moreover, the higher yield stress of n-l-AG ensures a more precise and consistent fibre dimensions. However, when pore size was evaluated (Figure 2(d),iv), scaffolds fabricated by depositing l-AG ink exhibited the smallest pore size. This reduction in pore size is due to the validated behaviour of the l-AG material ink to deposit fibres of greater diameter when exposed to a constant pressure, which leads to a narrowing of the pores. On the other hand, the n-l-AG was able to produce pores very close to the desired size. This is because the n-l-AG material faithfully reproduces the fibre dimensions, thereby achieving a pore size closer to the intended design. Overall, these tests provided a detailed assessment of the material's characteristics and their 3D printing performances. Results in Figure 2(e), highlight the ability of the tested material inks to faithfully reproduce the desired dimensions while also revealing differences in pore sizes, which can influence the properties of the resulting scaffolds. Notably, the n-l-AG material demonstrated superior capability in maintaining the desired pore size due to its accurate fibre reproduction, on the other hand, l-AG material showed the worst printability properties with respect to the other blends of materials. In summary, all the previous measurements provide critical insights into the performance and suitability of the materials for 3D bioprinting applications. The n-l-AG and h-AG materials, with their superior resistance to degradation, higher viscosity, and better printability, offer significant advantages in, reproducibility, maintaining scaffold structure and stability over time. For these reasons, l-AG was excluded for further testing as unsuitable for long-term culture and fabrication of the constructs.

The MOS3S platform was adapted to dispense a predefined volume of material ink in a multi-well plate in a controlled fashion. Initially, the spatial coordination of MOS3S was investigated to evaluate the feasibility of the use in high-throughput mode. Controlled dispensing of a set volume of material inks was carried out in a canonical 96-well plate dish (Figure 3(a)). A set of volumes ranging from 10 to 300 µL (Figure 3(b)) were deposited in a linear gradient, demonstrating the ability of the MOS3S platform to synchronise linear displacements and extrusion abilities. As shown in Figure 3(c), Video 2 and Video 3, further tests were carried out to demonstrate the ability of the MOS3S syringe pumps to deliver the desired volume with precision, as well as switching between different materials during the printing process. Furthermore, to evaluate the resolution of the deposition platform, the three syringe pumps were controlled to extrude specific volumes of 50 and 300 µL (Figure 3(d)) to assess the correlation between the desired and measured extruded volumes. Both for low and high volumes, the syringe pumps demonstrated good performance, with the extruded amount closely matching the target volumes, albeit slightly lower than the desired values. Specifically, pump one extruded 4% less material than targeted, pump two extruded 7% less, and pump three extruded 2% less with respect to the desired amount of volume. After identifying the syringe pump with the greatest error, further testing
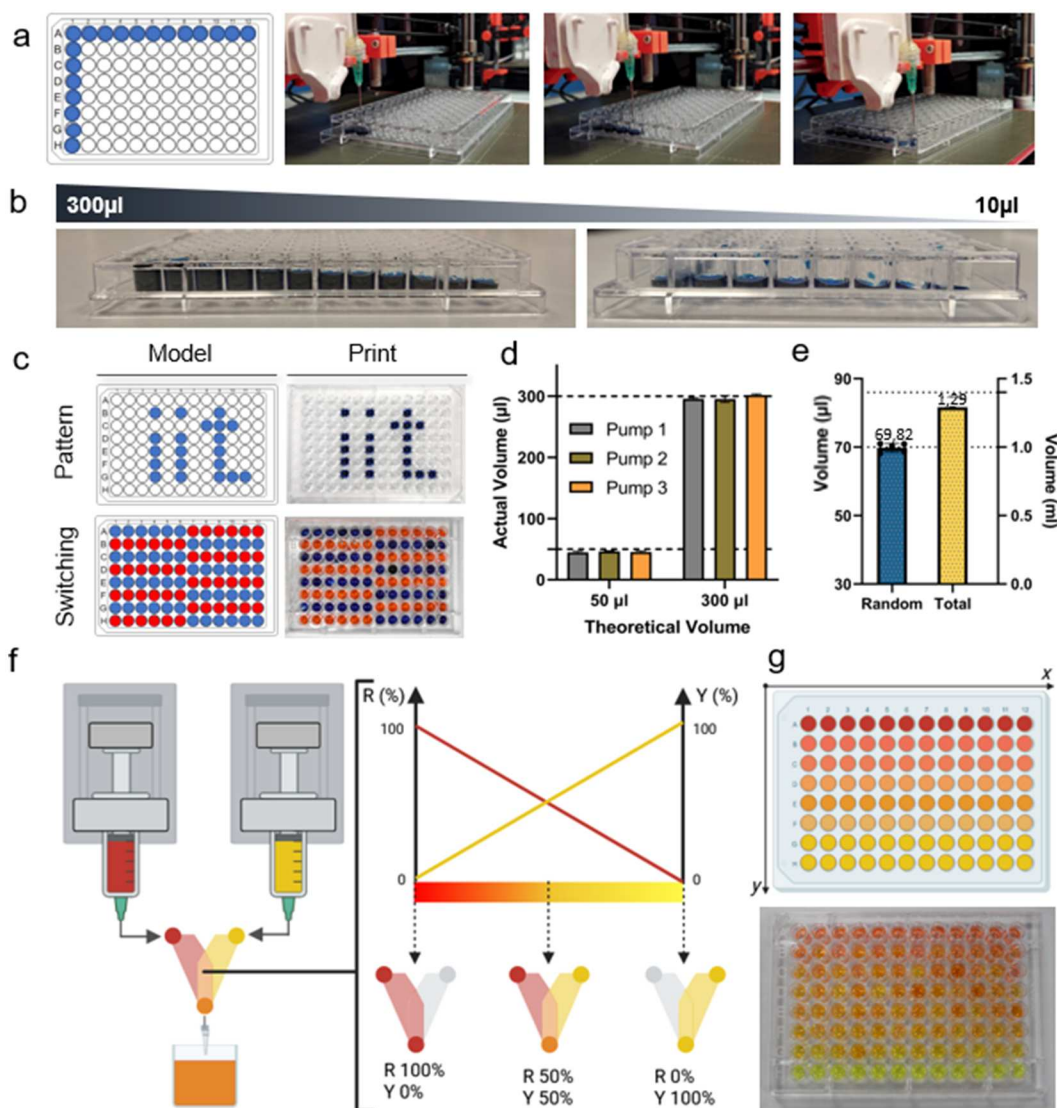
**Figure 3.** (a) Linear gradient deposition of volumes from 300 to 0 μL across wells A12 to H1, passing through A1, to test coordination between movement and extrusion. (b) Successful demonstration of the printer's capabilities for high-throughput applications controlling the extruded ink amount during the process (c) Arbitrary path definition and material switching during the continue printing process. (d) Volume extrusion accuracy test for 50 and 300 μL using three syringe pumps, showing close match between desired and actual volumes. (e) Test results of syringe pumps extruding 70 μL, shown in blue bar, in 20 repetitions, with a total ideal volume of 1.4 mL and an actual extruded volume of 1.29 mL shown with the yellow bar (f) Schematic of simultaneous operation of syringe pumps, showing synchronised flow control and compositional adjustment. (g) 96-well plate test showing linear gradient of component concentrations to validate precise control over material composition.

was conducted to assess its accuracy and precision. A total of 20 samples of 70 μL each were extruded, and 5 of these samples were randomly selected to calculate statistical measures. The mean volume extruded was 69.82 ± 3.45 μL, represented by the blue bar in Figure 3(e). Additionally, the total volume of these 20 samples was compiled, resulting in 1,29 mL extruded volume compared to the calculated 1,40 mL, corresponding to the yellow bar in Figure 3(e). This exhibited a 9% error for the least accurate pump. Consequently, subsequent experiments were performed using only the two more accurate and precise syringe pumps. Thus, the ability

of MOS3S to extrude two materials simultaneously was tested by tuning the percentage of the two components, as shown in Figure 3(f). The mixing of materials in this study occurs prior to deposition through the coaxial nozzle, where two different materials are combined in a three-way chip, ensuring thorough mixing via turbulence before extrusion. Although the focus of this work is on the applications of coaxial printing for multi-material constructs, detailed analysis of the mixing mechanism will be addressed in future studies. To manage simultaneous flows, MOS3S was programmed to control multiple flows concurrently. By synchronising

these flows, the printer was tuned to adjust the composition of the extruded fluid to achieve different concentrations of the two components. This capability was further validated in a 96-well plate test (Figure 3(g)), where the concentrations of the two components were varied linearly across the wells. These experiments underscore the advanced capabilities of the customised 3D bioprinting platform, showcasing its potential for complex scientific applications. After the conducted tests, it is evident that the performance of the 3D bioprinter is suitable for our purposes, confirming that it can effectively handle various material blends and high-throughput processes, despite minor deviations in extrusion accuracy.

The high-throughput system was utilised to investigate the drug release, which is critical for advancing therapeutic strategies [50,51] performing cellular function and differentiation [52,53]. For this reason, a drug-modelling compound typically used for assessing release dynamics (FITC-Dextran) was tested in combination with h-AG and n-l-AG [54]. The printhead of MOS3S can be equipped with a multi-extrusion system shown in Figure S3, with a coaxial nozzle, used to extrude bioink and crosslinking solution simultaneously, and a single nozzle to deposit a microfluidically-enhanced multi-material system, specifically designed for high-throughtput delivery. MOS3S equipped with a 405 nm lamp, was programmed to dispense controlled volume of liquid-state material inks to then crosslink the deposited materials by moving the well-plate of interest below the relative UV-source. The concentration of FITC-Dextran within the materials was set at 10 μg/mL. Consequently, a volume of 100 μL of each ink was extruded into a 96-well plate (Figure 4(b), Video 4) before undergoing cross-linked with Ru/SPS complex (Figure 4(c)). To monitor the release profile over time, samples were collected at multiple time points: 1, 2, 3, 6, 24, 48, 96, 12, 144 and 168 hours. For each time point, three replicate samples ($n = 3$) were isolated from different wells to ensure a statistical evaluation. The collected supernatant was then analysed for fluorescence emission, with excitation at a wavelength of 485 nm and acquired emission at 535 nm. To calculate the corresponding drug concentration from the fluorescence intensity, a linear regression equation was established using calibration samples of HBSS with known FITC-dextran concentrations ranging from 0 to 10 μg/mL with 1 μg/mL increments (Figure 4(d)). The resulting release profile was found consistent and controllable over time for both material inks (Figure 4(e),i). Following 168 hours of incubation in a temperature-controlled environment (37°C), the compound was not completely evacuated, with n-l-AG releasing 58% of the

loaded cargo and h-AG releasing 64% reaching a plateau. Nevertheless, the inclusion of nanoclay was found beneficial for the localisation of the loaded compound as the ultimate concentration localised within the n-l-AG was found significantly greater than the nanoclay-free ink. Moreover, Noticeably, the presence of nanoclay did not impair the rapid release of FITC-dextran as reported in a magnified view of the release profile (Figure 4(e),ii). Despite the initial burst release, these results validate our hypothesis of nanoclay inclusion to enhance drug retention – as reported in previous studies [26, 27, 55–57]. To visually quantify the discharged cargo, we carried out the release experiment using a higher FITC-Dextran concentration (1 mg/mL) than the one employed in the bioprinter-guided drug release experiment (10 μg/mL). In fact, the lower concentration did not produce sufficient fluorescent emission for detection via imaging devices, although it was measurable using the microplate reader thank to an integrated optical fibre delivering optimal sensitivity (typically $< 12 \cdot 10^{-18}$ mol). Thus, in order to provide a qualitative graphical representation of the release dynamics, a further investigation was conducted with the increased concentration. Subsequently, fluorescent images of both the sample and supernatant were captured at different time points (Figure S4a,b). As observed, the fluorescent intensity in the supernatant increased over time, while the fluorescent intensity within the sample decreased. Moreover, we quantified the fluorescence intensity of the samples by calculating the intensity percentage of pictures for both h-AG and n-l-AG, as shown in Figure S4c. The percentage of each sample is normalised on the maximum intensity emission recorded at the start of the experiment (hour 0). The n-l-AG samples exhibited higher fluorescent emission, indicating greater retention of FITC-Dextran compared to h-AG, as confirmed by our experimental results. The quantitative normalised intensity of the loaded samples (Figure S4d) was found significantly ($p<0.0001$) higher for nanoclay-based composites compared to clay-free controls, demonstrating the efficacy of n-l-AG in retaining loaded cargos. The primary objective was to qualitatively determine which material offered the highest drug retention capabilities to guide our material selection for subsequent experiments. Despite the variations in the geometrical design and the volume of materials tested, our qualitative analysis distinctly indicated that the n-l-AG blend showcased superior drug retention, making it the most suitable material for our studies. Consequently, based on the results collected from the drug release studies, the n-l-AG blend was selected as ideal material ink candidate for the engineering of the multi-functional 3D
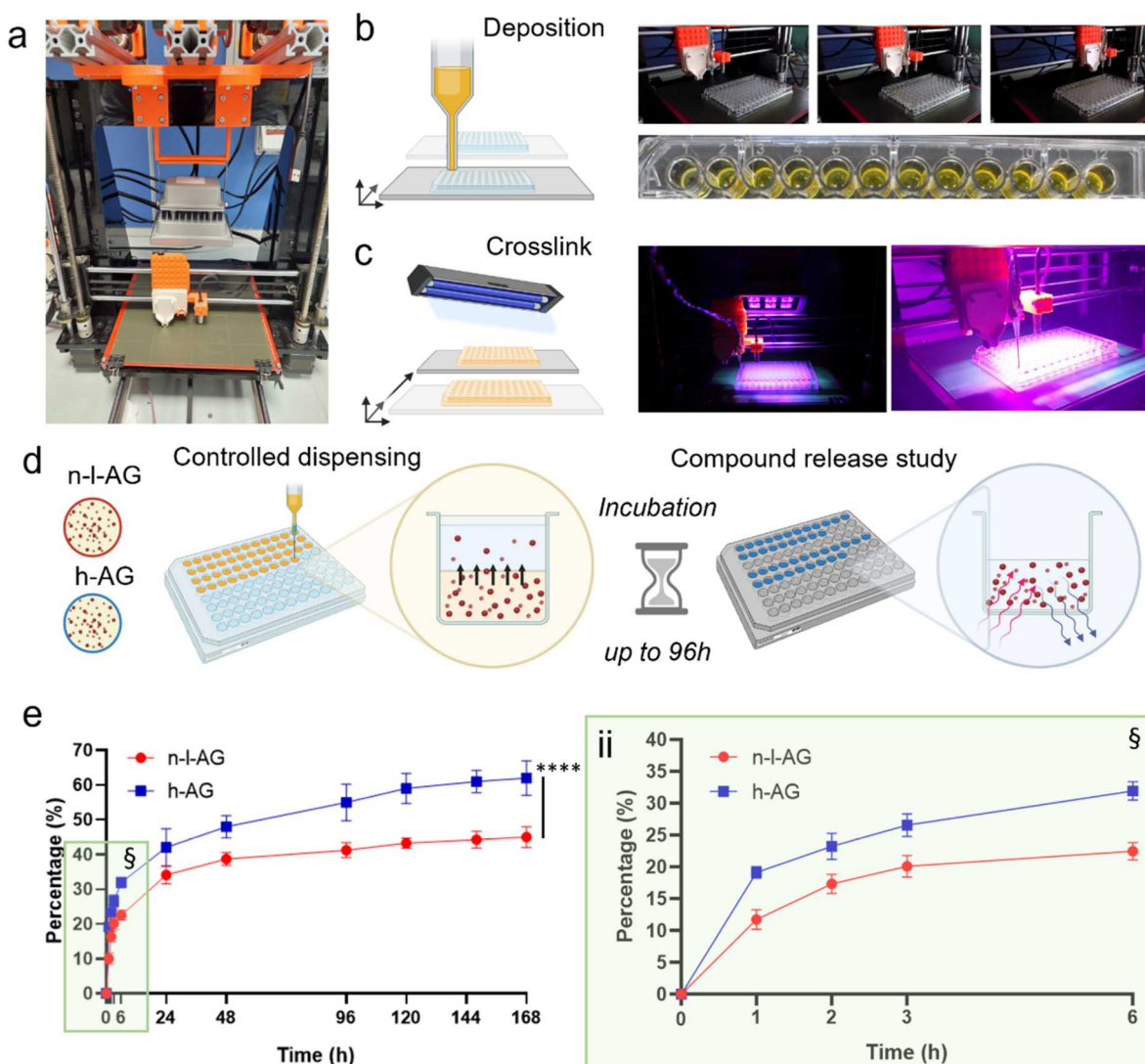
**Figure 4.** (a) Image of the customised 3D bioprinter, highlighting the print head and the UV lamp mounted at the top for crosslinking. (b) Photographs captured during the deposition of material into a 96-well plate. (c) Post-deposition phase, showing the activation of the lamp for crosslinking the material. (d) Schematic representation of the entire drug release experiment process, starting with the encapsulation of FITC-Dextran in h-AG and n-l-AG materials, followed by deposition into multiwells, crosslinking, addition of HBSS, sampling at specified time intervals, and measurement of fluorescence emission. (e) Graphs depicting the drug release concentration over time, showing that n-l-AG exhibits greater drug retention compared to h-AG. Mean ± S.D, $n$=5.

bioprinted high-throughput model (Figure 5). To demonstrate the ability to both 3D bioprint a cell-laden supporting platform and localise compounds within the construct of interest, a cancer model and a skeletal implant for tissue regeneration were engineered (Figure 5(a)). A multi-component 3D construct has been designed (Figure 5(b)) and biofabricated (Figure 5(c)) proving the ability of the MOS3S system to deliver a synergistic approach for 3D bioprinting and high-throughput technology. The scaffolds engineered with the combination of 3D bioprinting and high-throughput approach were fabricated with a specific structural design. The initial layers were printed with a pore size of 0.5 mm and a scaffold size of 9×9 mm to establish a

foundational support structure. Subsequent layers were printed with larger pore size, featuring a diameter of 3 mm. These were specifically designed to facilitate the insertion of drug-releasing ink droplets, which are composed of the same n-l-AG material used in the scaffold matrix. The array format was chosen to increase surface area contact with the culture medium, enhancing nutrient perfusion and facilitating the efficient exchange of nutrients and waste between the cells and their environment [58, 59]. This structure improves cellular behaviour, especially in dense tissue constructs where maintaining core viability is challenging. Additionally, the array format allowed our 3D bioprinting platform to precisely dispense material ink within
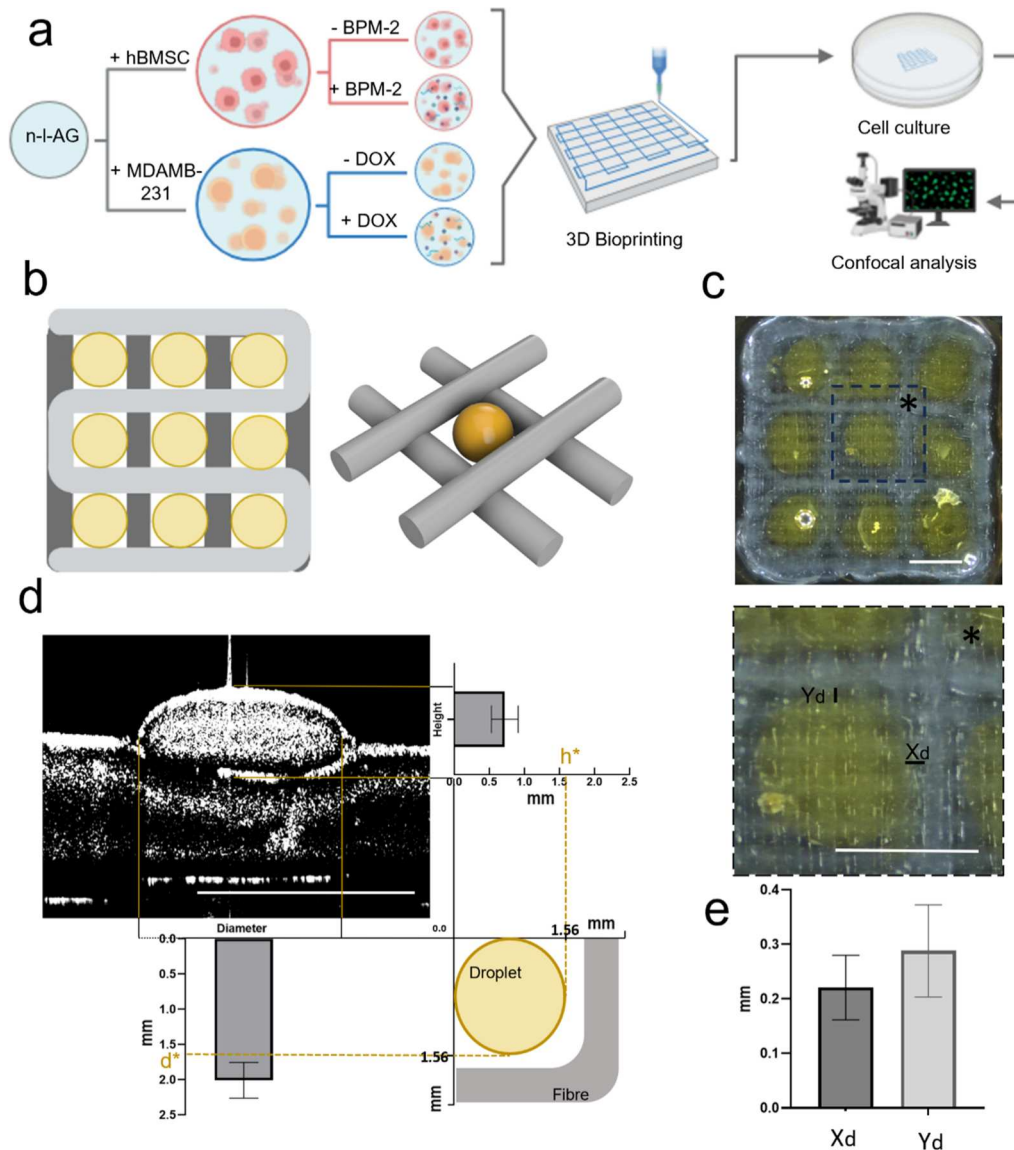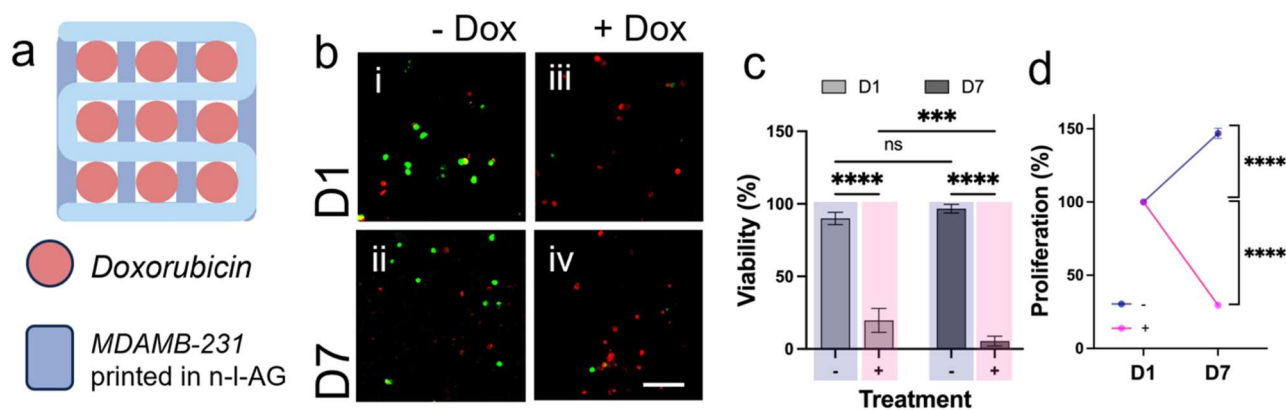
**Figure 5.** (a) Schematic representation of the process for creating bone model and skeletal substitute implants from n-l-AG material. HBMSCs and MDAMB-231 cells are added, with each cell type tested in implants without and with drugs (BMP-2 and doxorubicin, respectively). Implants are printed and analysed using confocal microscopy after cell culture. (b) Illustration of the implant structure, where the scaffold is designed with large pores to incorporate drug-releasing droplets using high-throughput techniques and are shown the geometric parameters of droplets. (c) Pictures of the printed scaffolds where the filament and the droplets are composed in n-l-AG. (d) Cross-sectional OCT image of a deposited droplet, and the graph illustrates the average diameter (1.09 ± 2.25 mm) and height (0.72 ± 0.19 mm) of droplets. (e) Distance between droplets on the X-axis (0.22 ± 0.06 mm) and Y-axis (0.29 ± 0.09 mm) indicating the precision of droplet placement. Scale bars: (c, d) 2 mm.

the large scaffold pores, creating localised compartments for better retention and distribution of biologics. The images presented in Figure 5(c–e) provide a detailed analysis of the droplets deposited within the scaffold. Figure 5(c) depicts a micrograph of a 3D printed scaffold demonstrating the displacement and diameter of the droplets. While Figure 5(d) displays a cross-sectional view of a droplet captured with OCT. The measured droplet diameter is 1.09 ± 0.25 mm, and the height is 0.72 ± 0.19 mm, based on 18 samples.

Additionally, graphs in Figure 5(e) depict the measured distances between droplets, with an X-axis spacing of 0.22 ± 0.06 mm and a Y-axis spacing of 0.29 ± 0.09 mm. These measurements confirm the precision and consistency of the droplet deposition process. The calculated droplet volume, approximated as an ellipsoid, aligns closely with the expected extruded volume to the minimum used, demonstrating the accuracy and reliability of the MOS3S printer. This level of printing capability not only supports the high quality of the

printed structures but also ensures that the MOS3S printer can accurately produce complex scaffolds, which is critical for their intended biological applications. Thus, scaffolds evaluated without drugs were still printed with droplets, albeit without active content, to maintain consistent structural integrity. To model a three-dimensional platform capable of resembling the effect of sustained exposure of anti-tumour drugs to cancerous tissue, breast cancer cells were encapsulated and printed in n-l-AG, while the therapeutic compound of interest was localised within the macro-porosity of the scaffold. MDAMB-231 cells were printed within n-l-AG scaffolds at a concentration of $3 \cdot 10^6$ cell/ml, with or without doxorubicin at concentration of 2µM in n-l-AG droplets (Figure 6(a)), to investigate drug efficacy and cellular response. Cell viability analysis (Figure 6(b,c)) showed that on day 1 (D1), viability in scaffolds without doxorubicin was 85%, increasing to 95% by day 7 (D7). In contrast, scaffolds with doxorubicin exhibited 25% viability at D1, decreasing to 8% at D7. Scaffold cellular density (Figure 6(d)) was assessed to determine cell proliferation with and without doxorubicin. By D7, untreated cells grew by 50%, while treated cells decreased by 70%. Furthermore, we conducted an additional experiment to evaluate the effects of controlled drug release respect a one-time dosage on cellular response within the printed structure. MDAMB-231 cells were printed at $3 \cdot 10^6$ cells/mL concentration in n-l-AG material ink. A one-time dosage of Doxorubicin at 2 µM was applied to the culture medium for 24 hours and subsequently removed. Cell viability and proliferation were assessed at D1 and D7, as illustrated in Figure S5a. The cell viability at D1 (Figure S5b) was significantly lower in the one-time dosage condition compared to the controlled release, due to the immediate availability of Doxorubicin in the culture medium, unimpeded by the retention properties of the scaffold. However, following an initial media change after 24 hours, viability increased by D7, as reflected by an observed leap in proliferation (Figure S5c). In contrast, the encapsulated Doxorubicin (Figure 6), released gradually over time, led to a reduction in proliferation, indicating that sustained drug release is more effective in inhibiting cell growth over extended periods compared to a discrete one-time dosage, possibly minimising side effects and damage to surrounding healthy tissues. This approach aligns with our goal of optimising the therapeutic effects while ensuring safety, particularly in potential *in vivo* applications where reducing systemic exposure is paramount [60–62]. Moreover, these findings highlight a significant difference between the two groups, validating our initial hypotheses and supported by further recent studies [63,64]. This drug-releasing cancer model provides a promising platform to investigate drug safety and efficacy on bioprinter cancer cells. Concomitantly, the nanoclay-based material ink was employed to engineer a bone substitute functionalised with compartmentalised BMP-2 (Figure 7). The n-l-AG was selected for the engineering of a bone substitute implant due to its lower and more prolonged release profile of BMP-2, which enhances the osteogenic differentiation of HBMSCs. This sustained release increases the treatment efficacy by providing a continuous supply of the growth factor, which is crucial for effective bone regeneration [65,66]. Additionally, it reduces inflammation in surrounding tissues, a key consideration for in vivo applications, ensuring a safer and more efficient healing process [67]. HBMSCs were



**Figure 6.** (a) Schematic representation of the scaffold architecture. Blue indicates n-l-AG printed fibres encapsulating MDAMB-231 cells, while red droplets represent DOX. Control scaffolds feature droplets without encapsulated drug. (b) Confocal microscopy images acquired at D1 and D7 for both drug-treated and untreated samples with and without DOX. (c) Viability at D1 and D7 of scaffolds treated with doxorubicin (in red) and untreated scaffolds (in blue). (d) Proliferation at D1 and D7 of scaffolds treated with DOX (in red) and untreated scaffolds (in blue). Scale bars: (b) 50µm. Mean ± S.D, $n=5$, ***$p<0.001$, ****$p<0.0001$.
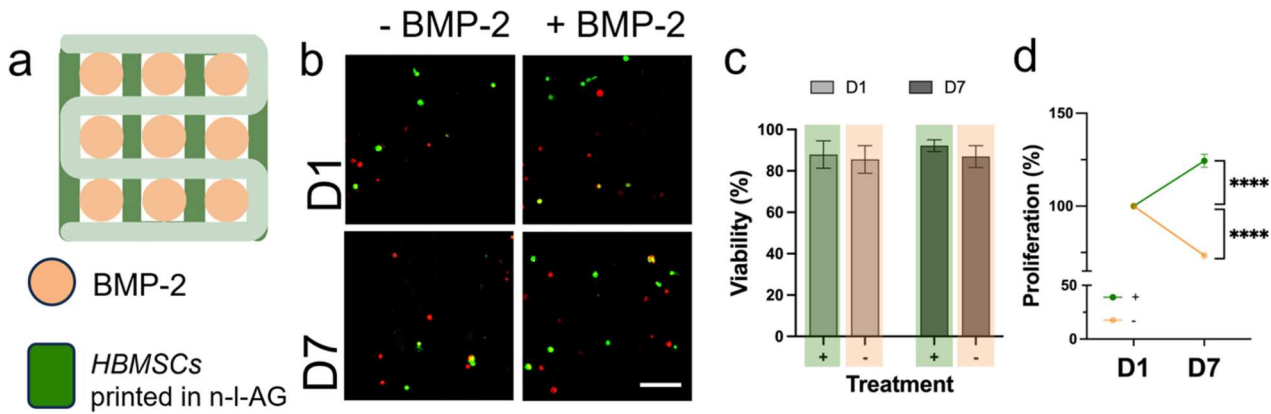
**Figure 7.** (a)Schematic representation of scaffold architecture. Blue denotes n-l-AG printed fibres encapsulating HBMSCs, while red droplets indicate BMP-2 presence. Control scaffolds feature droplets without encapsulated BMP-2. (b) Confocal microscopy images acquired at D1 and D7 for both BMP-2-treated and untreated samples. (c) Viability at D1 and D7 of scaffolds treated with BMP-2 (in red) and untreated scaffolds (in blue). (d) Proliferation at D1 and D7 of scaffolds treated with BMP-2 (in red) and untreated scaffolds (in blue). Scale bars: (b) 50μm. Mean ± S.D, $n=5$, ****$p<0.0001$.

embedded in n-l-AG material ink at a concentration of $3 \cdot 10^6$ cell/ml and deposited with or without the inclusion of BMP-2 inside the n-l-AG droplets at a concentration of 5 μl/ml dispensed compartments (Figure 7(a)). The resulting constructs were employed to assess the efficacy of the localised BMP-2 with associated improved cellular response. Cell viability (Figure 7(b,c)) indicated that scaffolds without BMP-2 had a viability of 82% on D1 and 83% on D7. In comparison, scaffolds with BMP-2 showed 85% viability at D1, which increased to 92% by D7. However, no significant difference due to the BMP-2 localisation was noted in cellular viability. Cell density within the scaffolds (Figure 7(d)) was evaluated to determine cell proliferation in the presence and absence of BMP-2. By D7, untreated cells exhibited a decline in proliferation, whereas the BMP-2 treated cells increased by 25%, possibly due to the increase in functional differentiation. In addition, experiments were conducted to study the biomarker alkaline phosphatase (ALP), an early marker of osteogenic differentiation [68,69], using scaffolds made of n-l-AG, both with and without the addition of BMP-2. Images related to these experiments are available in the supplementary files in Figure S6. On D1, the effect between the two conditions appeared similar. Given that BMP-2 has a long-term effect in promoting the sustained expression of ALP [70–72], by D7 there was a noticeably greater presence of ALP intensity in the scaffolds with BMP-2 compared to those without. Despite these observations, the concentrations of BMP-2 used did not yield a significant effect, indicating the need for further studies with higher concentrations. Nevertheless, this demonstrates that dispensing a localised compartment of BMP-2 onto the scaffolds

effectively enhances the osteogenic differentiation of HBMSCs, which is crucial for developing functional bone tissue in regenerative medicine applications.

To validate the induced-osteogenic differentiation of BMP-2 loading, a gene expression analysis during the initial 7 days of culture was conducted, as shown in supplementary Figure S7. The findings revealed that the expression of Runt-related transcription factor 2 (RUNX2), critical for initiating HBMSCs differentiation into osteoblasts, is notably higher in BMP-2 treated samples. This underscores the commencement of the differentiation process, corroborated by heightened activation of Osterix (OSX) in BMP2-treated samples. Furthermore, increased OSX expression regulates key proteins including type I collagen (COL1a1), osteocalcin (OCNv2), and alkaline phosphatase (ALP), facilitating extracellular matrix production and cell mineralisation. Particularly noteworthy is the enhanced expression of OCNv2 observed in BMP-2 treated samples, indicative of an advanced stage of osteogenic differentiation. The downregulation of ALP in BMP-2 treated samples, alongside reduced type I collagen expression, supporting and confirming the advanced mineralisation stage of BMP2-loaded compared to BMP2-free samples. This is further substantiated by ALP staining, which shows less intensity in BMP2-treated samples by day 7, indicating more advanced mineralisation compared to day 1 and BMP2-free samples. Lastly, BMP2 expression remains largely unchanged in both samples. This reflects the BMP2 immediate availability in treated samples thereby expediting the differentiation process. In the experimental design of this study, a lower cell density, specifically below $5 \cdot 10^6$ cells/ml, was employed to ensure high cell viability post-printing [73,74]. High cell

densities have been observed to alter viability, as increased cellular contact during the printing process and the subsequent encapsulation of a large number of cells can hinder effective nutrient exchange and waste removal within the lattice structure [75]. Moreover, although higher cell densities can enhance cell-to-cell communication, thereby potentially improving cellular proliferation and differentiation, the primary objective of these experiments was to evaluate the efficacy of specific drug agents – DOX for MDAMB-231 cells and BMP-2 for HBMSCs. This approach minimised the potential confounding effects of intense cellular interactions, allowing for a more precise impact of the drugs on cellular behaviour. These results, highlighting the significant differences with and without BMP-2, support our initial hypotheses and are consistent with findings from recently published studies [76,77]. The demonstrated efficacy of this drug-releasing bone substitute model suggests its potential for future research applications.

To evaluate the possible use in skeletal repair harnessing vascular ingrowth stimulating endochondral ossification, six fertilised eggs were employed for each experimental condition to host implanted hybrid construct over a period of 7 days (Figure 8(a)) [78]. Following incubation and ultimately implant extraction and imaging, VEGF-mediated vascular ingrowth was found prominent compared to the empty and the control groups (Figure 8(b)). This is to be expected due to the potent pro-angiogenic effect stimulated by the presence of localised VEGF compound [36,45]. To quantify afferent vasculature, a novel AI-assisted approach was developed to automatically screen for the number of afferent vessels (Chalkley score), as well as the diameter and the area occupied by the vessels (Figure 8(c–e)). The VEGF compartmentalisation in combination with the deposition of living HBMSCs was found beneficial for the increase in afferent vessels (Figure 8(c)) and diameter (Figure 8(d)) compared to the empty control, while eliciting no effect on the total area covered by the vessels
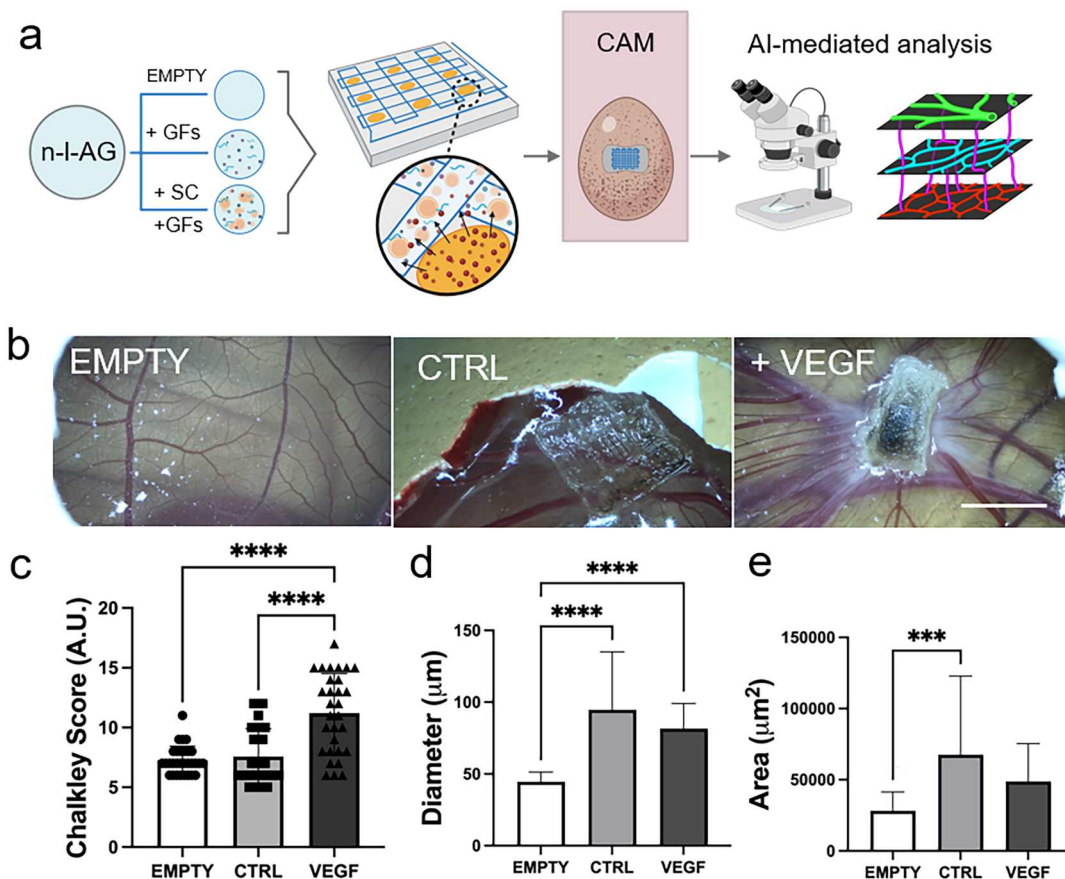


**Figure 8.** (a) Schematic representation of the experiment where two experimental conditions were tested using n-l-AG material. The first condition involved scaffolds of n-l-AG with encapsulated HBMSC, while the second condition involved the same material with HBMSC and scaffolds immersed in a solution containing BMP-2. These scaffolds were then implanted in CAM and analysed on day 14, with comparisons made against controls without scaffolds. (b) Photographs of the CAM with no scaffold (control) and the two experimental conditions. (c) Graphs derived from the analysis of the photographic images, showing the Chalkley score, vessel diameter, and the area covered by vascularisation. Scale bars: (b) 10 mm. Mean ± S.D, $n=5$, ***$p<0.001$, ****$p<0.0001$.

(Figure 8(e)), which, surprisingly, was found significantly greater in control implants. These results are possibly due to the rapid angiogenic potential of VEGF-loaded samples. The deposition and inclusion of VEGF compartments have driven a surge of new vessels that although increasing the overall afferent number, remain immature (small in diameter and area) for the short period of developmental incubation (7 days). A further investigation in an *in vivo* model is planned for further studies, which might elucidate the ultimate functionality of this new platform for relevant regenerative medicine purposes.

## Conclusions

3D bioprinting approaches have not yet demonstrated a scalable ability to compartmentalise compounds of interest with an efficient and reproducible approach. Herein, we have demonstrated that the combination of high-throughput dispensing and 3D bioprinting technologies can be harnessed to model cancer responses to clinically relevant drugs as well as modulate the response of stem cells to growth factors of interest. The use of nanoclay in combination with alginate-gelatin ink has been found beneficial for both printability and drug localisation, confirmed with the MOS3S system used either in 3D bioprinting or high-throughput dispensing mode. The use of this new nanoclay-enhanced ink allowed for the fabrication of lattice structures with enhanced resolution and print fidelity. Particularly, the dispensing of pre-defined volumes of inks validated with MOS3S confirmed the possibility to achieve tuneable delivery of controllable concentration of inks via microfluidic control within the bioprinted scaffold. This was in turn confirmed by the results obtained using the combination of the 3D bioprinting and high-throughput dispensing approaches, fabricating constructs that, for the first time, can influence angiogenesis based on the functionalisation of stem cell-laden constructs with growth factor compartments. Altogether, the findings presented here demonstrate the potential of the synergistic combination of microfluidic-based 3D bioprinting approach with high-throughput dispensing for the fine control of functional tissue fabrication and development.

## Acknowledgements

## Disclosure statement

## Data availability statement

## Ethics approval

## ORCID

*Salvatore D'Alessandro* http://orcid.org/0000-0001-7983-2085
*Biagio Palmisano* http://orcid.org/0000-0002-1287-5256
*Mara Riminucci* http://orcid.org/0000-0002-8643-9211
*Gianluca Cidonio* http://orcid.org/0000-0002-9445-6994

## References

[1] Iafrate L, Benedetti MC, Donsante S, et al. Modelling skeletal pain harnessing tissue engineering. Vitr Model. 2022;1:289–307. doi:10.1007/s44164-022-00028-7

[2] D'Antoni C, Mautone L, Sanchini C, et al. *Unlocking neural function with 3D in vitro models: a technical review of self-assembled, guided, and bioprinted brain organoids and their applications in the study of neurodevelopmental and neurodegenerative disorders.* Int J Mol Sci. 2023;24:10762. doi:10.3390/ijms241310762

[3] Burdis R, Kelly DJ. Biofabrication and bioprinting using cellular aggregates, microtissues and organoids for the engineering of musculoskeletal tissues. Acta Biomater. 2021;126:1–14. doi:10.1016/j.actbio.2021.03.016

[4] Mirshafiei M, Rashedi H, Yazdian F, et al. Advancements in tissue and organ 3D bioprinting: current techniques, applications, and future perspectives. Mater Des. 2024;240:112853. doi:10.1016/j.matdes.2024.112853

[5] D'Orazio M, Filippi J, Antonelli G, et al. Cells in the 3D Biomatrix on-chip: better mimicking the real micro-physiological system. Next Mater. 2024;5:100229. doi:10.1016/j.nxmate.2024.100229

[6] Bini F, Pica A, Marinozzi A, et al. A 3D model of the effect of tortuosity and constrictivity on the diffusion in mineralized collagen fibril. Sci. Rep. 2019;9:2658. doi:10.1038/s41598-019-39297-w

[7] Bhusal A, Dogan E, Nguyen HA, et al. Multi-material digital light processing bioprinting of hydrogel-based microfluidic chips. Biofabrication. 2022;14. doi:10.1088/1758-5090/ac2d78

[8] Ye W, Li H, Yu K, et al. 3D printing of gelatin methacrylate-based nerve guidance conduits with multiple channels. Mater Des. 2020;192:108757. doi:10.1016/j.matdes.2020.108757

[9] Grigoryan B, Paulsen SJ, Corbett DC, et al. Multivascular networks and functional intravascular topologies within biocompatible hydrogels. Science (80-.). 2019;364:458–464. doi:10.1126/science.aav9750

[10] Mohan TS, Datta P, Nesaei S, et al. 3D coaxial bioprinting: process mechanisms, bioinks and applications. Prog Biomed Eng. 2022;4:022003. doi:10.1088/2516-1091/ac631c

[11] Lee G, Kim SJ, Chun H, et al. Multilayered and heterogeneous hydrogel construct printing system with cross-linking aerosol. Biofabrication. 2021;13; doi:10.1088/1758-5090/ac25ca

[12] Liu W, Zhang YS, Heinrich MA, et al. Rapid continuous multimaterial extrusion bioprinting. Adv Mater. 2017;29:1–8. doi:10.1002/adma.201604630

[13] Shim JH, Lee JS, Kim JY, et al. Bioprinting of a mechanically enhanced three-dimensional dual cell-laden construct for osteochondral tissue engineering using a multi-head tissue/organ building system. J Micromech Microeng. 2012;22:085014. doi:10.1088/0960-1317/22/8/085014

[14] Meng F, Meyer CM, Joung D, et al. 3D bioprinted in vitro metastatic models via reconstruction of tumor microenvironments. Adv. Mater. 2019;31:e1806899. doi:10.1002/adma.201806899

[15] Rakib Hasan Khan M, Shankar Hazra R, Nair G, et al. Cellulose nanofibers as scaffold-forming materials for thin film drug delivery systems. Int J Pharm. 2022;627:122189. doi:10.1016/j.ijpharm.2022.122189

[16] Zhang B, Morgan M, Teoh XY, et al. Recent advances in 3D printing for in vitro cancer models. J Appl Phys. 2024;135:140701. doi:10.1063/5.0200726

[17] Monteiro CF, Custódio CA, Mano JF. Bioengineering a humanized 3D tri-culture osteosarcoma model to assess tumor invasiveness and therapy response. Acta Biomater. 2021;134:204–214. doi:10.1016/j.actbio.2021.07.034

[18] Kanwar S, Vijayavenkataraman S. 3D printable bone-mimicking functionally gradient stochastic scaffolds for tissue engineering and bone implant applications. Mater. Des. 2022;223:111199. doi:10.1016/j.matdes.2022.111199

[19] Cheah CK, Chua KF, Leong CMC, et al. Development of a tissue engineering scaffold structure library for rapid prototyping. Part 1: investigation and classification. Int J Adv Manuf Technol. 2003;21:291–301.

[20] Mohammadi S, Cidonio G. Unravelling hierarchical patterning of biomaterial inks with 3d microfluidic-assisted spinning: a paradigm shift in bioprinting technologies. Nature. 2023;388:539–547.

[21] Naing MW, Chua CK, Leong KF, et al. Fabrication of customised scaffolds using computer-aided design and rapid prototyping techniques. Rapid Prototyp J. 2005;11:249–259. doi:10.1108/13552540510612938

[22] Mohammadi S, D'Alessandro S, Bini F, et al. Development of a microfluidic-assisted open-source 3D bioprinting system (MOS3S) for the engineering of hierarchical tissues. HardwareX. 2024;18:e00527. doi:10.1016/j.ohx.2024.e00527

[23] Koons GL, Mikos AG. Progress in three-dimensional printing with growth factors. J Control Release. 2019;295:50–59. doi:10.1016/j.jconrel.2018.12.035

[24] Miao G, Liang L, Li W, et al. 3D bioprinting of a bioactive composite scaffold for cell delivery in periodontal tissue regeneration. Biomolecules. 2023;13:1062. doi:10.3390/biom13071062

[25] Li H, Mao B, Zhong J, et al. Localized delivery of metformin via 3D printed GelMA-nanoclay hydrogel scaffold for enhanced treatment of diabetic bone defects. J Orthop Transl. 2024;47:249–260. doi:10.1016/j.jot.2024.06.013

[26] Cidonio G, Dodhia VH, Iafrate L, et al. Clay nanofiller enhances and stabilises a new injectable human bone extracellular matrix scaffold for skeletal regeneration. Mater Today Commun. 2024;39:109082. doi:10.1016/j.mtcomm.2024.109082

[27] Kim YH, Kanczler JM, Lanham S, et al. Biofabrication of nanocomposite-based scaffolds containing human bone extracellular matrix for the differentiation of skeletal stem and progenitor cells. Bio-Design Manuf. 2024;7:121–136. doi:10.1007/s42242-023-00265-z

[28] Lim KS, Schon BS, Mekhileri NV, et al. New visible-light photoinitiating system for improved print fidelity in gelatin-based bioinks 2016;2:1752–1762. doi:10.1021/acsbiomaterials.6b00149

[29] Sun M, Sun X, Wang Z, et al. Synthesis and properties of gelatin methacryloyl (GelMA) hydrogels and their recent applications in load-bearing tissue. Polymers (Basel). 2018;10:1290. doi:10.3390/POLYM10111290

[30] Costantini M, Idaszek J, Szöke K, et al. 3D bioprinting of BM-MSCs-loaded ECM biomimetic hydrogels for in vitro neocartilage formation. Biofabrication. 2016;8:035002. doi:10.1088/1758-5090/8/3/035002

[31] Xiang Y, Wang W, Gao Y, et al. Production and characterization of an integrated multi-layer 3D printed PLGA/GelMA scaffold aimed for bile duct restoration and detection. Front Bioeng Biotechnol. 2020;8:1–14. doi:10.3389/fbioe.2020.00971

[32] Marcotulli M, Tirelli MC, Volpi M, et al. Microfluidic 3D printing of emulsion ink for engineering porous functionally graded materials. Adv Mater Technol. 2023;8:1–12. doi:10.1002/admt.202201244

[33] Ribeiro A, Blokzijl MM, Levato R, et al. Assessing bioink shape fidelity to aid material development in 3D bioprinting. Biofabrication. 2018;10:014102. doi:10.1088/1758-5090/aa90e2

[34] Robey PG, Kuznetsov SA, Riminucci M, et al. Bone marrow stromal cell assays – in vitro and in vivo. Nature. 2018;388:539–547.

[35] Ahlfeld T, Cidonio G, Kilian D, et al. Development of a clay based bioink for 3D cell printing for skeletal application.

Biofabrication. 2017;9:034103. doi:10.1088/1758-5090/aa7e96

[36] Cidonio G, Alcala-Orozco CR, Lim KS, et al. Osteogenic and angiogenic tissue formation in high fidelity nano-composite laponite-gelatin bioinks. Biofabrication. 2019;11:035027. doi:10.1088/1758-5090/ab19fd

[37] Kirillov A, Mintun E, Ravi N, et al. Segment anything. 4015–4026.

[38] Meeting AG, Orleans N, Cancer I, et al. Calendar of forthcoming meetings. **2002**, 2002–2003.

[39] Chen A, Wang W, Mao Z, et al. Multimaterial 3D and 4D bioprinting of heterogenous constructs for tissue engineering. Adv. Mater. 2023;36:e2307686. doi:10.1002/adma.202307686

[40] Rastogi P, Kandasubramanian B. Review of alginate-based hydrogel bioprinting for application in tissue engineering. Biofabrication. 2019;11:042001. doi:10.1088/1758-5090/ab331e

[41] Aldana AA, Valente F, Dilley R, et al. Development of 3D bioprinted GelMA-alginate hydrogels with tunable mechanical properties. Bioprinting. 2021;21:e00105. doi:10.1016/j.bprint.2020.e00105

[42] Zhang X, He Y, Huang P, et al. A novel mineralized high strength hydrogel for enhancing cell adhesion and promoting skull bone regeneration in situ. Compos. Part B Eng. 2020;197:108183. doi:10.1016/j.compositesb.2020.108183

[43] Fang X, Xie J, Zhong L, et al. Biomimetic gelatin methacrylamide hydrogel scaffolds for bone tissue engineering. J Mater Chem B. 2016;4:1070–1080. doi:10.1039/C5TB02251G

[44] Allen NB, Abar B, Johnson L, et al. 3D-Bioprinted GelMA-gelatin-hydroxyapatite osteoblast-laden composite hydrogels for bone tissue engineering. Bioprinting. 2022;26:e00196. doi:10.1016/j.bprint.2022.e00196

[45] Cidonio G, Glinka M, Kim YH, et al. Nanoclay-based 3D printed scaffolds promote vascular ingrowth ex vivo and generate bone mineral tissue in vitro and in vivo. Biofabrication. 2020;12:035010. doi:10.1088/1758-5090/ab8753

[46] Cidonio G, Cooke M, Glinka M, et al. Printing bone in a gel: using nanocomposite bioink to print functionalised bone scaffolds. Mater Today Bio. 2019;4:100028. doi:10.1016/j.mtbio.2019.100028

[47] Kim YH, Kanczler JM, Lanham S, et al. Biofabrication of nanocomposite-based scaffolds containing human bone extracellular matrix for the differentiation of skeletal stem and progenitor cells. Bio-Design Manuf. 2024;7:121–136. doi:10.1007/s42242-023-00265-z

[48] Mouser VHM, Melchels FPW, Visser J, et al. Yield stress determines bioprintability of hydrogels based on gelatin-methacryloyl and gellan gum for cartilage bioprinting. Biofabrication. 2016;8:1–13. doi:10.1088/1758-5090/8/3/035003

[49] Gillispie GJ, Copus J, Uzun-Per M, et al. The correlation between rheological properties and extrusion-based printability in bioink artifact quantification. Mater. Des. 2023;233:112237. doi:10.1016/j.matdes.2023.112237

[50] Pagnotta G, Kalia S, Di Lisa L, et al. Progress towards 3D bioprinting of tissue models for advanced drug screening: in vitro evaluation of drug toxicity and drug metabolism. Bioprinting. 2022;*27*, e00218; doi:10.1016/j.bprint.2022.e00218

[51] Ma X, Liu J, Zhu W, et al. 3D bioprinting of functional tissue models for personalized drug screening and in vitro disease modeling. J Vet Behav Clin Appl Res. 2018;132:235–251. doi:doi:10.1016j.addr.2018.06.011.

[52] De la Vega L, Abelseth L, Sharma R, et al. 3D bioprinting human-induced pluripotent stem cells and drug-releasing microspheres to produce responsive neural tissues. Adv NanoBiomed Res. 2021;1:2000077. doi:10.1002/anbr.202000077

[53] Fu Z, Hai N, Zhong Y, et al. Printing GelMA bioinks: a strategy for building in vitro model to study nano-particle-based minocycline release and cellular protection under oxidative stress. Biofabrication. 2024;16. doi:10.1088/1758-5090/ad30c3

[54] Luanda A, Badalamoole V. Past, present and future of biomedical applications of dextran-based hydrogels: a review. Int J Biol Macromol. 2023;228:794–807. doi:10.1016/j.ijbiomac.2022.12.129

[55] Cidonio G, Glinka M, Kim YH, et al. Nanoclay-Based 3D printed scaffolds promote vascular ingrowth ex vivo and generate bone mineral tissue in vitro and in vivo. Biofabrication. 2020;12:035010. doi:10.1088/1758-5090/ab8753

[56] Man K, Barroso IA, Brunet MY, et al. Controlled release of epigenetically-enhanced extracellular vesicles from a GelMA/nanoclay composite hydrogel to promote bone repair. Int J Mol Sci. 2022;23:832. doi:10.3390/ijms23020832

[57] Ahlfeld T, Cidonio G, Kilian D, et al. Development of a clay based bioink for 3D cell printing for skeletal application. Biofabrication. 2017: 9:034103. doi:10.1088/1758-5090/aa7e96

[58] Melchels FPW, Tonnarelli B, Olivares AL, et al. The influence of the scaffold design on the distribution of adhering cells after perfusion cell seeding. Biomaterials. 2011;32:2878–2884. doi:10.1016/j.biomaterials.2011.01.023

[59] Nguyen TD, Olufemi EK, Sikavitsas VI, et al. Scaffolds with a high surface area-to-volume ratio and cultured under fast flow perfusion result in optimal $O_2$ delivery to the cells in artificial bone tissues _ enhanced reader. MDPI - Biomater Bone Tissue Eng. 2019;9:2381. doi:10.3390/app9112381.

[60] Emerich DF, Snodgrass P, Lafreniere D, et al. Sustained release chemotherapeutic microspheres provide superior efficacy over systemic therapy and local bolus infusions. Pharm Res. 2002;19:1052–1060. doi:10.1023/A:1016434926649

[61] Bai X, Smith ZL, Wang Y, et al. Sustained drug release from smart nanoparticles in cancer therapy A comprehensive review. Micromachines (Basel). 2022;13(10):1623. doi:10.3390/mi13101623

[62] Zhu J, Gao R, Wang Z, et al. Sustained and targeted delivery of self-assembled doxorubicin nonapeptides using PH-responsive hydrogels for osteosarcoma chemotherapy. Pharmaceutics. 2023;15(2):668. doi:10.3390/pharmaceutics15020668

[63] Flores-Torres S, Peza-Chavez O, Kuasne H, et al. Alginate-gelatin-matrigel hydrogels enable the development and multigenerational passaging of patient-derived 3D bioprinted cancer spheroid models. Biofabrication. 2021;13; doi:10.1088/1758-5090/abdb87

[64] Lee K-S, Lee M-G, Kwon Y-S, et al. Arctigenin enhances the cytotoxic effect of doxorubicin in MDA-MB-231 breast cancer cells. Int J Mol Sci. 2020;21(8):2997. doi:10.3390/ijms21082997

[65] Poldervaart MT, Wang H, van der Stok J, et al. Sustained release of BMP-2 in bioprinted alginate for osteogenicity in mice and rats. PLoS One. 2013;8:e72610. doi:10.1371/journal.pone.0072610

[66] Percival KM, Paul V, Husseini GA. Recent advancements in bone tissue engineering: integrating smart scaffold technologies and Bio-responsive systems for enhanced regeneration. Int J Mol Sci. 2024;25:6012. doi:10.3390/ijms25116012

[67] Nguyen V, Meyers CA, Yan N, et al. BMP-2-Induced bone formation and neural inflammation. J Orthop. 2017;14:252–256. doi:10.1016/j.jor.2017.03.003

[68] Zhou P, Shi JM, Song JE, et al. Establishing a deeper understanding of the osteogenic differentiation of monolayer cultured human pluripotent stem cells using novel and detailed analyses. Stem Cell Res Ther. 2021;12:1–16. doi:10.1186/s13287-020-02006-w

[69] Gromolak S, Krawczenko A, Antończyk A, et al. Biological characteristics and osteogenic differentiation of ovine bone marrow derived mesenchymal stem cells stimulated with FGF-2 and BMP-2. Int J Mol Sci. 2020;21:1–22. doi:10.3390/ijms21249726

[70] Ingwersen LC, Frank M, Naujokat H, et al. BMP-2 long-term stimulation of human pre-osteoblasts induces osteogenic differentiation and promotes transdifferentiation and bone remodeling processes. Int J Mol Sci. 2022;23:3077. doi:10.3390/ijms23063077

[71] Martin-Iglesias S, Milian L, Sancho-Tello M, et al. BMP-2 enhances osteogenic differentiation of human adipose-derived and dental pulp stem cells in 2D and 3D in vitro models. Stem Cells Int. 2022;2022:4910399. doi:10.1155/2022/4910399

[72] Montagna G, Pani G, Flinkman D, et al. Long-term osteogenic differentiation of human bone marrow stromal cells in simulated microgravity: novel proteins sighted. Cell Mol Life Sci. 2022;79:536. doi:10.1007/s00018-022-04553-2.

[73] Nicodemus GD, Bryant SJ. Cell encapsulation in biodegradable hydrogels for tissue engineering applications. Tissue Eng - Part B Rev. 2008;14:149–165. doi:10.1089/ten.teb.2007.0332

[74] Lim KS, Schon BS, Mekhileri NV, et al. New visible-light photoinitiating system for improved print fidelity in gelatin-based bioinks. ACS Biomater Sci Eng. 2016;2:1752–1762. doi:10.1021/acsbiomaterials.6b00149

[75] Cidonio G, Glinka M, Dawson JI, et al. The cell in the ink: improving biofabrication by printing stem cells for skeletal regenerative medicine. Biomaterials. 2019;209:10–24. doi:10.1016/j.biomaterials.2019.04.009

[76] Jiang F, Qi X, Wu X, et al. Regulating macrophage-MSC interaction to optimize BMP-2-induced osteogenesis in the local microenvironment. Bioact Mater. 2023;25:307–318. doi:10.1016/j.bioactmat.2023.02.001

[77] Love SA, Gultian KA, Jalloh US, et al. Mesenchymal stem cells enhance targeted bone growth from injectable hydrogels with BMP-2 peptides. J Orthop Res. 2024;42:1599–1607. doi:10.1002/jor.25798

[78] Cidonio G, Cooke M, Glinka M, et al. Printing bone in a gel: using nanocomposite bioink to print functionalised bone scaffolds. Mater Today Bio. 2019;4:100028. doi:10.1016/j.mtbio.2019.100028.